

# Drug-membrane permeability across chemical space

Roberto Menichetti, Kiran H. Kanekal, and Tristan Bereau\*  
*Max Planck Institute for Polymer Research, 55128 Mainz, Germany*

Unraveling the relation between the chemical structure of small drug-like compounds and their rate of passive permeation across lipid membranes is of fundamental importance for pharmaceutical applications. The elucidation of a comprehensive structure-permeability relationship expressed in terms of a few molecular descriptors is unfortunately hampered by the overwhelming number of possible compounds. In this work, we reduce a priori the size and diversity of chemical space to solve an analogous—but smoothed out—structure-property relationship problem. This is achieved by relying on a physics-based coarse-grained model that reduces the size of chemical space, enabling a comprehensive exploration of this space with greatly reduced computational cost. We perform high-throughput coarse-grained (HTCG) simulations to derive a permeability surface in terms of two simple molecular descriptors—bulk partitioning free energy and  $pK_a$ . The surface is constructed by exhaustively simulating all coarse-grained compounds that are representative of small organic molecules (ranging from 30 to 160 Da) in a high-throughput scheme. We provide results for acidic, basic and zwitterionic compounds. Connecting back to the atomic resolution, the HTCG predictions for more than 500,000 compounds allow us to establish a clear connection between specific chemical groups and the resulting permeability coefficient, enabling for the first time an inverse design procedure. Our results have profound implications for drug synthesis: the predominance of commonly-employed chemical moieties narrows down the range of permeabilities.

## I. INTRODUCTION

The passive permeation of small molecules across lipid membranes offers not only physico-chemical insight but also crucial pharmaceutical information about drug-membrane thermodynamics.<sup>1</sup> It probes the timescale of translocation due to a concentration gradient of the drug, without active cellular mechanisms (Fig. 1). A detailed understanding of the underlying structure-property relationships between drug chemistry and passive-permeation thermodynamics, though of great interest for drug development, is still lacking.

Structure-property relationships are often tackled by means of high-throughput screening experiments: (i) a large number of compounds are probed with respect to the property of interest by individual measurements or calculations; (ii) the relationship between structure and property is empirically learned by means of statistical algorithms.<sup>2–4</sup> While structure-property relationships thus formally rely on both the breadth and quality of the data, as well as the accuracy of the statistical model, the common bottleneck in the pharmaceutical sciences often arises from the former.

Even though in vivo techniques probe drug-membrane interactions in all the intricacies of the cellular environment, the experimental cost and complexity make them poorly suited for high-throughput screening.<sup>6</sup> It is instead the development of in vitro techniques that have helped in expanding passive-permeation databases.<sup>7,8</sup> Unfortunately, limited aggregate data has been made publicly available thus far. The resulting statistical models—such as quantitative structure-property relationships (QSPR) or machine learning—typically rely on  $10^2$  to  $10^4$  datapoints only.<sup>9–11</sup> The question follows: how representative can these samples be, when the size of drug chemical space is estimated at  $10^{60}$ ?<sup>12</sup> The tendency of

these statistical models to depend significantly on individual outliers strongly suggest overfitting—these models lack transferability across chemical space.<sup>10</sup> The small-dataset problem is typically aggravated by the compounds’ poor diversity.<sup>13</sup>

As a complementary approach to experimental measurements, physics-based modeling provides a robust strategy to predict passive permeation in silico.<sup>10,14</sup> The inhomogeneous solubility-diffusion model<sup>15,16</sup> considers the concentration gradient of a solute molecule across an interface to yield a permeability coefficient,  $P$ .<sup>17</sup> This results in a spatial integral normal to the interface,  $z$ , of the potential of mean force (PMF),  $G(z)$ , and local diffusivity,  $D(z)$ ,

$$P^{-1} = \int dz \frac{\exp[\beta G(z)]}{D(z)}, \quad (1)$$

with  $\beta = 1/k_B T$ . Eq. 1 highlights the two key parameters that contribute to the rate of passive permeation of a compound: its hydrophobicity, quantified by the PMF, together with the local diffusivity. Practically,  $G(z)$  and  $D(z)$  are commonly extracted from enhanced-sampling classical molecular dynamics simulations. Grounding the problem within the statistical mechanics of a concentration flux diffusing through an interface combined with conformational sampling from physically-motivated force fields can offer unprecedented insight. We stress that current experimental techniques have yet to resolve  $G(z)$ —computer simulations thus remain the gold standard to estimate Eq. 1. Unfortunately, adequate conformational sampling remains computationally daunting at the atomistic level, even for a small rigid molecule crossing a single-component lipid membrane: roughly  $10^5$  CPU-hours per compound limit this strategy to up to  $\sim 10$  different molecules per study.<sup>18–21</sup> When combined with the

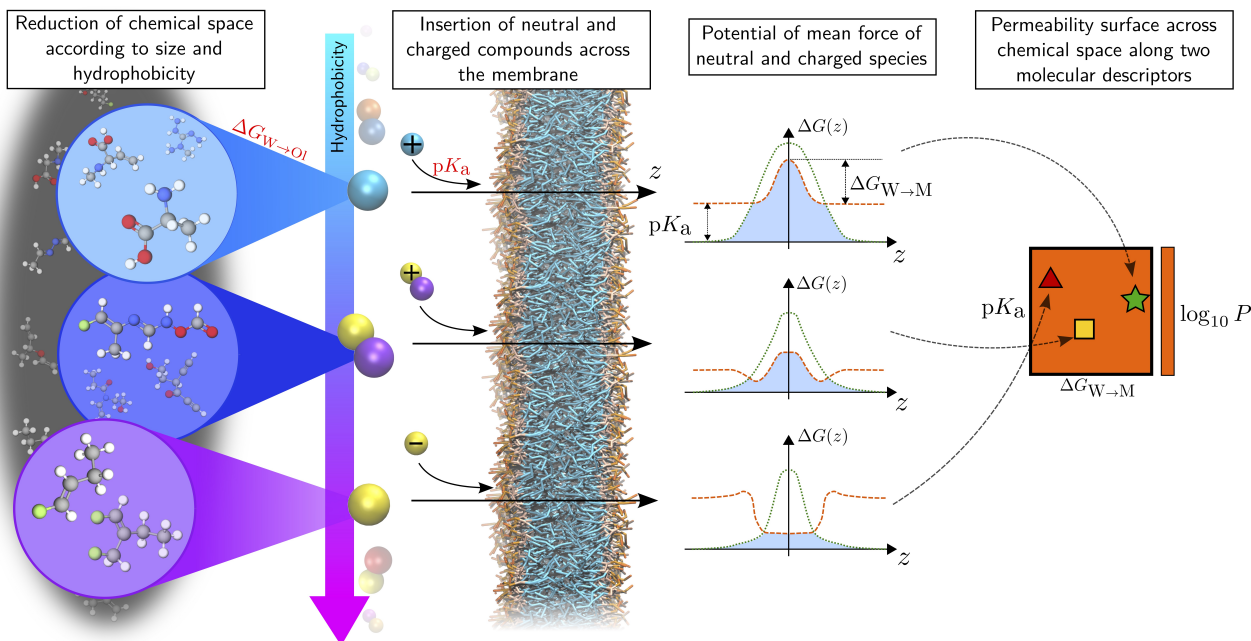


FIG. 1. From left to right: Coarse-graining reduces the size of chemical space, such that many small molecules of similar size and hydrophobicity get mapped to the same representation.<sup>5</sup> For each molecule, we model its passive translocation across a lipid bilayer (water not shown for clarity). The thermodynamics of the system is characterized by the potential of mean force (PMF), evaluating both the neutral and charged species, shifted according to the compound’s  $pK_a$ . The major dependence of the PMF on the water/octanol partitioning and the  $pK_a$  motivates these as molecular descriptors to construct a permeability surface (Eq. 1). These two molecular descriptors, also highlighted in red, are experimental quantities directly fed into the physics-based simulations to yield a parameter-free estimation of the permeability coefficient.

overwhelming size of chemical space, these figures hinder short-term prospects of running atomistic simulations at high throughput, thereby hampering the elucidation of the underlying structure-property relationships.

Structure-property relationships effectively project down chemical complexity on a few molecular descriptors that map to the property of interest.<sup>22,23</sup> Inferring these maps typically relies on a statistical analysis over many measurements, identifying a *smooth* (i.e., low-dimensional) connection between structure and property. In this work we propose an alternative strategy: rather than smoothing this connection a posteriori, we enforce it a priori. We still rely on physics-based models but reduce their resolution to efficiently interpolate across chemistry, while ensuring accurate thermodynamics by construction. This enables a high-throughput approach for two reasons: (i) the reduced representation significantly speeds up every simulation, and (ii) the interpolation across chemistry effectively reduces the size of chemical space. Solving the structure-property relationship problem for the reduced model proves significantly more tractable, and allows the identification of a permeability surface as a function of simple molecular descriptors. We further connect back to the original problem by means of a large-scale analysis of our predictions.

The abovementioned reduced models, better known as coarse-grained (CG) models, lump together several atoms

into a bead.<sup>24,25</sup> While defined in terms of fewer degrees of freedom, coarse-graining remains physics-based and can be combined with rigorous free-energy calculations. Here, we rely on the CG Martini model, which has shown useful to simulating a wide variety of biomolecular systems.<sup>26–28</sup> In Martini, a small set of bead types encodes how small organic fragments partition between solvents of different polarity, thus ensuring robust thermodynamics at complex interfaces,<sup>28</sup> while cutting down the computational costs by three orders of magnitude.<sup>29</sup>

The parametrization of a molecule at the CG level thus consists of a collection of Martini beads, each representing a specific chemical group. Constructing a CG molecule can be streamlined into a systematic procedure,<sup>30</sup> so as to emulate the molecule’s overall shape and hydrophobicity. The small set of bead types leads to a degeneracy in the representation: many molecules of similar shapes and hydrophobicity map to the same CG parametrization (Fig. 1). Such a many-to-one mapping generates a significant reduction in the size of chemical space—further lowering the computational investment by an additional  $10^3 - 10^4$ . The few bead types involved leads to a dramatic reduction in the combinatorial explosion of chemistry, easing the construction of *all* CG small molecules up to a certain size (Fig. 1).<sup>5</sup> This addresses the poor-diversity issues that synthetic databases typically face, facilitating a representative coverage of sub-

sets of chemical space projected primarily along size and hydrophobicity. Recently, these properties allowed us to predict the PMF of drug-membrane partitioning for an unprecedented 511,427 small molecules—several orders of magnitude beyond what was previously available.<sup>5</sup> In terms of accuracy we showed that the CG model achieves a mean-absolute error of 0.8 kcal/mol to predict bulk water/octanol partitioning free energies,<sup>30</sup> translating to a 1.4 kcal/mol error along a PMF.<sup>5</sup> We further stress that these errors are evaluated across a significant subset of the chemistry of small organic molecules, while atomistic results are too scarce to make such estimates. For the present work, our error estimates roughly translate to an accuracy of  $1 \log_{10}$  unit in the permeability coefficient, validated across an extensive set of structurally-distinct compounds against both atomistic simulations and experimental measurements (see Supporting Information (SI)).

In this work, we use high-throughput coarse-grained (HTCG) simulations to cover a subset of chemical space both efficiently and broadly. Unlike conventional high-throughput screening protocols that require an arbitrary selection of compounds, we consider *all* coarse-grained representations up to a threshold size, mapping to most small organic molecules ranging from 30 to 160 Da. This comprehensive exploration allows us to systematically investigate the effect of hydrophobicity and  $pK_a$  on the permeation rate (Fig. 1), unlike previous studies limited to a handful of compounds.<sup>18–21</sup> Our methodology offers a unique approach to construct a two-dimensional surface describing the permeability of a small molecule across a lipid membrane (Fig. 1). The molecular descriptors are here motivated by the physics of the permeation process, i.e., the interplay between diffusivity and solubility (Eq. 1). Because the diffusivity was shown to be rather insensitive to chemical detail,<sup>18</sup> we focus on the potential of mean force,  $G(z)$ . We have recently shown that the key features of  $G(z)$  can be reconstructed simply from the bulk-partitioning free energy.<sup>5</sup> By further accounting for the contribution of different protonation states, we also express the permeability surface in terms of its acid dissociation constant in water,  $pK_a$ . In the following we focus on acidic and basic compounds, while the SI further discusses zwitterions. These surfaces allow for a rapid, *simulation-free* prediction of drug permeability starting from key molecular properties. The accuracy is roughly on par with explicit CG simulations due to compensating errors between the two methods.

Extracting permeability surfaces from the CG simulations allows us to connect back to the original structure-property relationship problem. Our analysis of over 500,000 small molecules mapping to the investigated CG representations unveils the role played by representative functional groups in the permeability coefficient, enabling inverse molecular design. The link drawn here has profound implications for drug synthesis: favoring the incorporation of certain chemical groups (e.g., carboxylic groups) will reduce the range of accessible permeabilities

of the final compound.

## II. RESULTS AND DISCUSSION

While drug permeation is known to depend on lipid composition,<sup>21</sup> in this work we only consider a single-component bilayer made of 1,2-dioleoyl-*sn*-glycero-3-phosphocholine (DOPC). The permeability coefficient,  $P$ , is readily estimated from the PMF and diffusivity profile (Eq. 1). The PMFs are extracted from HTCG simulations of *all* CG representations made of one and two beads, mapping to a representative subset of small organic molecules in the range 30–160 Da.<sup>5</sup> For compounds capable of (de)protonating, we also model the corresponding charged species. For convenience, we distinguish the  $pK_a$  of a chemical group as being either acidic ( $apK_a$ ) or basic ( $bpK_a$ ), which quantifies the propensity of a *neutral* compound to deprotonate or protonate, respectively. The effective permeability coefficient is constructed by a combination of the two PMFs (Fig. 1), shifted according to the compound’s  $pK_a$  in water, see Methods.<sup>31,32</sup> The diffusivity profile is estimated from reference atomistic simulations.<sup>18</sup>

### A. Permeability surfaces

Fig. 2 displays the computed drug-membrane permeability as a function of two drug parameters: its  $pK_a$  in water and water/membrane partitioning free energy,  $\Delta G_{W \rightarrow M}$ . The latter corresponds to the free energy difference between insertion in bulk water and the membrane-bilayer midplane. Though we have shown this quantity to correlate extremely well with the experimentally-accessible water/octanol partitioning free energy,  $\Delta G_{W \rightarrow O1}$ ,  $\Delta G_{W \rightarrow M}$  displays enhanced transferability across CG molecular sizes.<sup>5</sup> Indeed, HTCG simulations of single-bead or two-bead CG compounds lead to identical permeability surfaces, except for the range of  $\Delta G_{W \rightarrow M}$  covered (compare Fig. S4 with Fig. 2).

Fig. 2 displays smooth permeability surfaces as a function of the drug’s acidic and basic  $pK_a$  value in water. The  $\log_{10}$  scale of the permeability surfaces indicates the wide timescale variations these molecular parameters exert on the thermodynamic process. For both panels, the horizontal behavior indicates that larger permeabilities are obtained toward the left—more hydrophobic compounds—while polar molecules experience more difficulties crossing the lipid bilayer, leading to a drastic reduction in  $P$ . The effect is compounded by (de)protonation: panel (a) across the vertical axis describes the effect of the compound’s  $apK_a$  in water onto  $P$ . Extremely strongly acidic molecules ( $apK_a \lesssim 2$ ) effectively remain charged across the membrane interface, leading to prohibitively large free energies along the PMF, such that their rate of permeation is strongly suppressed. Increasing  $apK_a$  shows a significant increase in

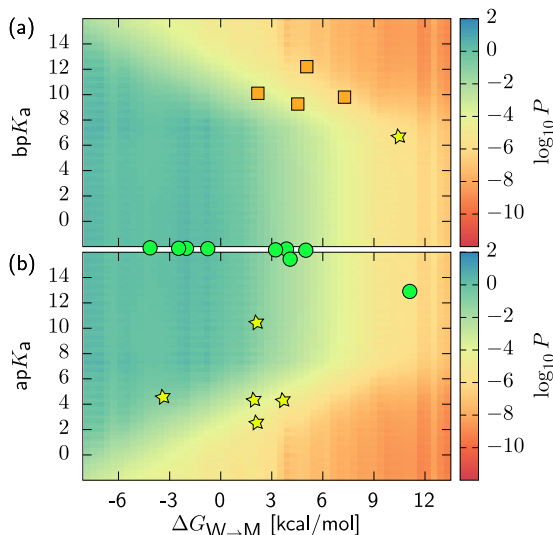


FIG. 2. Permeability surfaces ( $\log_{10}$  scale) calculated from HTCG simulations as a function of two small-molecule descriptors: the (a) basic or (b) acidic  $pK_a$  in water and the water/membrane partitioning free energy,  $\Delta G_{W \rightarrow M}$ . Cooler (warmer) colors correspond to faster (slower) permeating molecules. The intersection between the two surfaces corresponds to compounds that effectively always remain neutral. Green circles, yellow stars, and orange squares correspond to deviations from atomistic simulations within 0.5, 1.3, and 2.2 log units, respectively (SI).

$P$ , up to  $apK_a \approx 7$ , beyond which  $P$  plateaus. This stabilization is due to the competition between neutral and charged PMFs, where the charged PMF is shifted to increasingly larger values, and therefore never contributes significantly compared to the more attractive neutral PMF. Of particular interest are the strong acids ( $2 \lesssim apK_a \lesssim 7$ ), which neutralize upon entering the membrane, effectively enhancing the permeability coefficient as compared to a compound that remains charged across the interface. An approximately symmetric behavior can be observed when switching from acidic to basic compounds (panel (b)). The impact of both  $apK_a$  and  $bpK_a$  on the permeability coefficient becomes even more pronounced in the case of zwitterions (Fig. S5), where high permeation rates are only obtained for compounds containing both weak acidic *and* basic chemical groups.

The permeability surface also displays a comparison against atomistic simulations<sup>18,19,31</sup> for several compounds (symbols in Fig. 2). These points provide a validation of our methodology—we report a mean absolute error of 1.0  $\log_{10}$  unit across the two molecular descriptors—with additional information included in the SI (also against experimental data). Most importantly, the few datapoints highlight the extremely limited exploration of chemical space using *in silico* simulations at an atomistic resolution.

## B. Functional-group localization on the permeability surfaces

To better elucidate how the chemical structure impacts the permeability coefficient, we consider a large database of small organic molecules from combinatorial chemistry: the generated database (GDB).<sup>33,34</sup> It consists of a large set of stable molecules up to 10 heavy atoms made of the chemical elements C, O, N, and F, saturated with H. We pointed out how transferable coarse-grained models effectively reduce the size of chemical space by lumping many molecules into one coarse-grained representation.<sup>5</sup> This allows us to associate the abovementioned one- and two-bead CG permeability results to  $5 \times 10^5$  molecules. The distinction made between compounds that reduce to CG molecules made of a single bead (“unimers”) from those made of two beads (“dimers”) effectively amounts to a segregation between molecular weights.<sup>5</sup> We populate the permeability surfaces with these compounds—projecting them onto the two molecular descriptors:  $pK_a$  and water/octanol partitioning free energy  $\Delta G_{W \rightarrow O1}$ . By coarse-graining every single compound, we establish a map between chemical structure and its CG thermodynamic property.

Fig. 3 displays the chemical-space coverage of GDB compounds onto the molecular descriptors. For all panels, we have colored the points in terms of the permeability calculated using HTCG simulations. Top and bottom panels distinguish between  $bpK_a$  and  $apK_a$ , while left and right denote unimers and dimers, respectively. We first note that the cloud of points is not uniformly distributed, but is instead centered around zero in  $\Delta G_{W \rightarrow O1}$ . An increase in the molecular weight of the compound (left to right in Fig. 3) opens up new regions of chemical space, as we observe a significant broadening of the distribution along the water/octanol axis. This naturally arises due to the extensivity of the water/octanol partitioning, the more complex combinatorics of atoms involved, and the additional presence of five-membered rings.

Unlike bulk partitioning, the  $pK_a$  of a compound is not significantly impacted by aggregate behavior, but is instead dominated by one or a few specific chemical groups capable of (de)protonating. As such, we investigated the presence of chemical groups representative of a subset of chemical space. The regions in blue highlight a chemical group that is predominant, appearing in at least 50% of the molecules in that subset. Detailed statistics pertaining to the frequency of specific functional groups in each of the blue regions is provided in the SI. The localization of chemical groups remains largely similar from unimers to dimers (e.g., carboxylic group). Our high-throughput analysis offers an intuitive visualization of the link between chemistry and permeabilities via the  $pK_a$ . Fig. 3 reflects that oxygen-containing functional groups are generally more likely to be proton donors, whereas nitrogen-containing functional groups can serve as either proton donors or acceptors.<sup>35</sup> At low

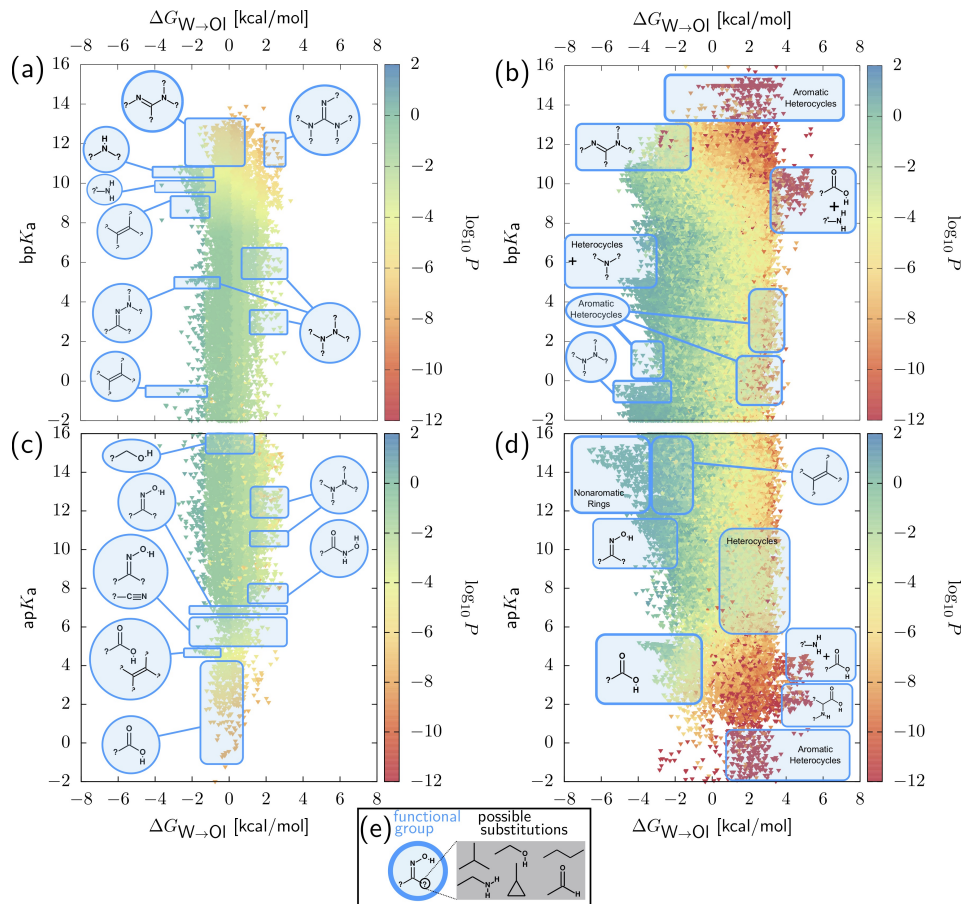


FIG. 3. Chemical-space coverage of GDB projected onto  $pK_a$  and water/octanol partitioning free energies,  $\Delta G_{W \rightarrow O}$ . Basic and acidic  $pK_a$  are shown in panels (a,b) and (c,d), respectively. Panels (a,c) and (b,d) describe the coverage corresponding to coarse-grained unimers and dimers, respectively. Regions highlighted in light blue display several representative chemical groups. Substitutions denoted by “?” correspond to either H or a substitution starting with an alkyl or aryl carbon, while “?\*” only corresponds to substitutions that begin with an alkyl carbon. (e) Our analysis clusters molecules containing both a predominant functional group (blue), but also one or several substitutions (black), of which only a few possibilities are shown.

$apK_a$  values, we mainly see carboxylic groups transitioning to nitrogen-containing functional groups (e.g., oxime derivatives) as we increase the  $apK_a$ . Contrastingly, the  $bpK_a$  chemical coverage displays no predominant oxygen-containing functional groups. Notable exceptions are the zwitterionic amino acid-like compounds and certain aromatic heterocyclic compounds shown in Fig. 3, which have both a low  $apK_a$  and a high  $bpK_a$ . These functional groups largely contribute to the chemical coverage of zwitterions (Fig. S5b).

### C. Linking functional groups and the permeability surface enables molecular design

Fig. 3 enables a robust ad hoc method for both direct and inverse molecular design. The direct route amounts to estimating the permeability coefficient given a chemical structure. Fig. 3 simply requires an estimate for

the two molecular descriptors,  $pK_a$  and  $\Delta G_{W \rightarrow O}$ , either from experiments or prediction algorithms.<sup>32,36</sup> More interestingly, our results allow us to focus on specific regions of chemical space compatible with a desired permeability coefficient. We effectively reduce the high dimensionality of chemical space by projecting down onto our molecular descriptors and identifying key scaffolds.

Fig. 3 offers a simple route at an inverse design procedure. For example, if designing a small molecule of 3 to 5 heavy atoms (i.e., mapping to a CG unimer) that requires a  $\log_{10} P$  of  $-1.0$ , Fig. 3c suggests molecules containing either a terminal hydroxyl group or an oxime group. Indeed, small alcohols such as propanol and butanol match this target (Fig. S8), although we are not aware of relevant experimental studies containing small oxime derivatives. Interestingly, we can also predict how small chemical changes will affect permeability: a change that impacts hydrophobicity (e.g., through heteroatom substitutions) will smoothly shift the compound horizontally on

the surface. On the other hand, the introduction of new (de)protonatable groups might lead to large jumps on the surface, dictated by the strongest acid or base present in the molecule. The different behavior across the horizontal and vertical axes is due to the extensive and intensive characters of the descriptors, respectively.

Critically, Fig. 3 shows remarkable transferability *outside* the range of compounds used in the screening. For example, while salicylate is made up of 10 heavy atoms, its aromatic ring leads to a four-bead representation. CG simulations using this parametrization result in  $\log_{10} P = -4.21$  (Fig. S6 and Table S1), deviating only one  $\log_{10}$  unit from the atomistic results (highlighted as one of the symbols in Fig. 2).<sup>18</sup> Alternatively, we can easily read off the permeability from the surface: the carboxylic group is the main contributor for its descriptors  $\text{ap}K_a = 2.8$  and  $\Delta G_{W \rightarrow O1} = -2.7$  kcal/mol (Fig. 3). This results in a *simulation-free* prediction for  $\log_{10} P$  of  $-3.72$ , less than two log units away from the atomistic results. The discrepancy between the four-bead representation and the dimer surface we rely on is the main source of errors: we have observed a systematic shift between  $\Delta G_{W \rightarrow O1}$  and  $\Delta G_{W \rightarrow M}$  as a function of the number of CG beads.<sup>5</sup> An even more challenging test case involved ibuprofen (206 Da, significantly outside our range of molecular weights), for which both CG simulations and the surface prediction yield an accuracy within 1  $\log_{10}$  unit within the atomistic results (symbol in Fig. 2, Fig. S6, and Table S1).

We verified this consistent accuracy between explicit CG simulations and simulation-free surface predictions across two dozen small molecules—both in and out of the range of molecular weights considered (Fig. S7 and Table S1). Although one would expect higher accuracy from explicit simulations, we observe compensating errors between the discretization of partitioning free energies and the smoothing of the surface. The transferability beyond the initial molecular weight considered speaks to the robustness of our physics-based approach. This feature contrasts radically with statistical methods that fit experimental data, such as QSPR: the transferability of a QSPR model hinges upon potential biases in the training dataset. Given the small dataset sizes available from experiments and the wider range of molecular weights, QSPR models tend to be limited to chemistries very close to those used in training.<sup>37,38</sup> On the other hand, the HTCG method systematically spans a wide region of chemical compound space without resorting to parameter tuning, offering accurate predictions even beyond the range of molecular weight considered.

#### D. Impact of functional-group localization on bioavailability

The projection of the GDB database onto the two molecular descriptors provides a low-dimensional representation of chemical-space coverage. Interestingly,

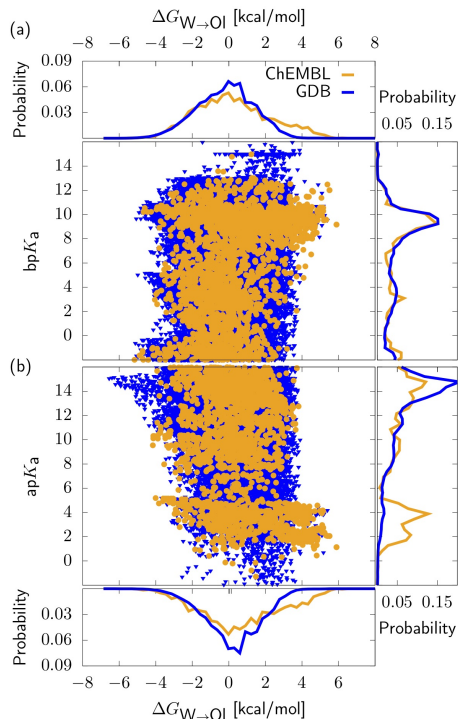


FIG. 4. Comparison of the chemical-space coverage of the combinatorial GDB and synthetic ChEMBL databases, projected onto (a) basic or (b) acidic  $\text{p}K_a$  and water/octanol partitioning free energy,  $\Delta G_{W \rightarrow O1}$ . The coverages are further projected down along a single variable on the sides. Note the significant differences between the GDB and ChEMBL distributions along the  $\text{ap}K_a$  in panel (b).

this helps compare its breadth and variety with other databases. In particular, we focus on ChEMBL: a database of synthesized compounds.<sup>39</sup> We prune ChEMBL to only retain compounds roughly compatible in size with the compounds in GDB (up to 10 heavy atoms), as well as H, C, O, N, and F elements only. Fig. 4 displays the coverage of both GDB and ChEMBL onto the molecular descriptors. Here again, panels (a) and (b) distinguish acidic and basic ionizing groups. We first note that ChEMBL displays a much smaller number of datapoints, illustrating the minuscule ratio of stable compounds that have been synthesized.<sup>12</sup> Overall the two databases cover remarkably similar regions of this chemical surface. However, a projection of the distributions along the individual axes indicates a statistically-significant difference for  $\text{ap}K_a$ : synthesized compounds strikingly overrepresent compounds with low  $\text{ap}K_a$  values (from 2 to 4). We find a significant overrepresentation of carboxylic groups in ChEMBL: 90% of the compounds in the range  $0 < \text{ap}K_a < 6$  contain such a group. This well-known bias in drug design<sup>40</sup> can readily be rationalized: Synthesizing compounds that include carboxylic groups will offer relatively strong acidity as well as an

improved ability to hydrogen bond—a dominant interaction in most biomolecular processes. Our results introduce further implications: the overrepresentation of carboxylic groups will effectively narrow down the range of permeability coefficients. This limitation will be further compounded by the necessity of a drug candidate to show high aqueous solubilities, and the delicate interplay existing between these two properties,<sup>41</sup> overall affecting the compounds’ bioavailability.

### III. CONCLUSIONS

We present the prediction of membrane-permeability coefficients for an unprecedented number and chemical range of small organic molecules across a single-component DOPC lipid bilayer. Rather than tackling the original structure-property relationship problem head-on, we work with physics-based reduced models that smoothly interpolate across chemistry, thereby reducing the size of chemical space. Critically, we do not arbitrarily select compounds to be screened, but instead systematically consider *all* coarse-grained representations that map to small organic molecules ranging from 30 to 160 Da. Coarse-grained permeability predictions were extensively validated against both atomistic simulations and experimental measurements for structurally-diverse compounds. The high-throughput coarse-grained (HTCG) simulation approach used here compounds more efficient conformational sampling and reduction in chemical space, offering an overall speedup of  $\sim 10^6$  compared to atomistic simulations. This enables a systematic exploration of the link between chemical structure and permeability coefficient. To this end we construct a smooth surface as a function of two molecular descriptors: the  $pK_a$  and water/membrane partitioning free energy,  $\Delta G_{W \rightarrow M}$ . The many orders of magnitude covered by the surface indicate the significant impact of the small molecule’s chemistry onto the thermodynamic process. The surfaces illustrate how strong acids and bases limit the loss of permeability for charged compounds. Having solved the reduced structure-property mapping allows us to connect back to the original, higher-dimensional problem. We identify dominant functional groups representative of chemical regions in the permeability surface. The identification of functional groups linking to the permeability coefficient effectively provides robust structure-property relationships for drug-membrane permeation, and the means to perform inverse molecular design. Finally, we show how the apparent bias of synthetic databases toward carboxylic groups can have deleterious effects on the accessible range of permeability coefficients, and thus on bioavailability. All in all, our HTCG approach offers a complementary approach to *in vitro* high-throughput screening, providing much larger numbers of compounds (510,000 in this study) than currently available in public databases. The much larger dataset size will help statistical models (e.g., QSPR) reach improved transferability.

In analogy to rapidly-growing interests in generating *in silico* databases of electronic properties,<sup>42,43</sup> we expect HTCG to have a broad impact in efficiently mapping the relevant low-dimensional surfaces that link chemical structure to thermodynamic properties.

## IV. METHODS

### A. Molecular dynamics simulations

Molecular dynamics simulations in this work were performed in GROMACS 4.6.6<sup>44</sup> and with the Martini force field,<sup>26–28</sup> relying on the standard simulation parameters.<sup>45</sup> The integration time step was  $\delta t = 0.02 \tau$ , where  $\tau$  is the model’s natural unit of time dictated by the units of energy  $\mathcal{E}$ , mass  $\mathcal{M}$  and length  $\mathcal{L}$ ,  $\tau = \mathcal{L}\sqrt{\mathcal{M}/\mathcal{E}}$ . Sampling from the  $NPT$  ensemble at  $P = 1$  bar and  $T = 300$  K was obtained by means of a Parrinello-Rahman barostat<sup>46</sup> and a stochastic velocity rescaling thermostat,<sup>47</sup> with coupling constants  $\tau_P = 12 \tau$  and  $\tau_T = \tau$  respectively. We relied on the INSANE building tool<sup>48</sup> to generate a membrane of  $\approx 36$  nm<sup>2</sup> containing  $N = 128$  DOPC lipids (64 per layer),  $N' = 1890$  water molecules,  $N'' = 190$  antifreeze particles,<sup>27</sup> and enough counterions to neutralize the box. The system was subsequently minimized, heated up, and equilibrated.

The potential of mean force  $G(z)$  of each compound was determined by means of umbrella sampling.<sup>49</sup> We employed 24 simulation windows with harmonic biasing potentials ( $k = 240$  kcal/mol/nm<sup>2</sup>) centered every 0.1 nm along the normal to the bilayer midplane. In each of them, two solute molecules were placed in the membrane in order to increase sampling and alleviate leaflet-area asymmetry.<sup>31,50</sup> The total production time for each umbrella simulation was  $1.2 \cdot 10^5 \tau$ . We then estimated the free-energy profiles by means of the weighted histogram analysis method.<sup>51–53</sup>

### B. Permeability coefficients

The permeability coefficient is obtained from the potential of mean force  $G(z)$  and local diffusivity  $D(z)$  in the resistivity  $R(z) = \exp[\beta G(z)]/D(z)$ , see Eq. 1. For compounds with multiple protonation states, both neutral and charged species contribute to the total flux, leading to the total resistivity  $R_T$  given by<sup>18</sup>  $R_T(z)^{-1} = R_N(z)^{-1} + R_C(z)^{-1}$ , where  $R_N$  and  $R_C$  are the resistivities of the neutral and charged species, respectively. In calculating these quantities in the case of a single (de)protonation reaction, one has to offset the corresponding PMFs  $G_N(z)$  and  $G_C(z)$  by the free-energy difference for the acid/base reaction in bulk water<sup>31</sup>

$$G_{\text{base}} = G_{\text{acid}} + k_B T (pK_a - \text{pH}) \ln 10, \quad (2)$$

see Fig. 1, where we systematically consider neutral  $\text{pH} = 7.4$ . Beyond the distinction between acid and base, we consider both neutral and charged species (Fig. 1): (i) a neutral acid deprotonates into a charged conjugate base (acidic  $\text{p}K_{\text{a}}$  or  $\text{ap}K_{\text{a}}$ ) and (ii) a neutral base protonates into a charged conjugate acid (basic  $\text{p}K_{\text{a}}$  or  $\text{bp}K_{\text{a}}$ ). The extension to zwitterions, in which two consecutive protonation and deprotonation reactions occur in different chemical groups leaving the molecule globally neutral, is discussed in the SI.

Estimation of the local diffusivity,  $D(z)$ , using the CG simulations is a priori problematic given the tendency of these models to inconsistently accelerate the dynamics.<sup>54</sup> On the other hand, atomistic simulations showed that the diffusivity across a DOPC bilayer was virtually independent of the chemistry of the solute.<sup>18</sup> We used this profile in the present calculations. We stress that the local diffusivity only provides a logarithmic correction to  $\log_{10} P$  (see Eq. 1), and therefore has limited impact—a variation well within 1  $\log_{10}$  unit depending on the diffusivity profile. More details can be found in Secs. S2 and S6 of the SI.

### C. Permeability surfaces

We obtained the permeability surfaces presented in Figs. 2 and S4 by first determining the PMF  $G(z)$  for *all* possible neutral combinations of one and two CG beads, 119 in total. For each of them we then determined  $G(z)$  for its charged counterparts, amounting to a total of 232 additional compounds. All PMF calculations required less than  $10^5$  CPU hours, on par with the typical computational time needed to run a *single* compound at an atomistic resolution.<sup>10</sup> At the CG level, protonating (deprotonating) a neutral chemical group amounts to replacing the bead type with a positive (negative) charge. We assume that the (de)protonation reaction always occurs in the chemical fragment represented by the more polar bead, and select the bead accordingly. In Sec. S3 of the SI, we justify this approach by analyzing the  $\text{p}K_{\text{a}}$  distribution for various CG bead types. By combining neutral and charged PMFs, we calculated the permeability coefficient of every compound as a function of the  $\text{ap}K_{\text{a}}$  ( $\text{bp}K_{\text{a}}$ ) every 0.2  $\text{p}K_{\text{a}}$  unit, and projected the results on the  $(\Delta G_{\text{W} \rightarrow \text{M}}, \text{p}K_{\text{a}})$  plane. The data consisted of a discrete set of permeabilities densely covering the partitioning free-energy axis located at the  $\Delta G_{\text{W} \rightarrow \text{M}}$  of each CG compound, and were finally interpolated on a grid with gaussian weights resulting in the surfaces shown in Fig. 2 and Fig. S4.

### D. Chemical space coverage

Prediction of the water/octanol partitioning on both chemical databases considered in this work, GDB<sup>33,34</sup> and ChEMBL,<sup>39</sup> was performed by means of the neural network ALOGPS.<sup>36</sup>  $\text{ap}K_{\text{a}}$  and  $\text{bp}K_{\text{a}}$  predictions of neutral compounds were provided by the Calculator Plugin of CHEMAXON MARVIN.<sup>32</sup> The mean absolute error associated with the two prediction algorithms are 0.36 kcal/mol<sup>36</sup> and 0.86 units,<sup>55</sup> respectively. The aggregate predictions of water/octanol partitioning and  $\text{p}K_{\text{a}}$  on both databases required roughly  $10^2$  CPU hours. Functional groups were identified using the CHECKMOL package.<sup>56</sup> 511,427 molecules were coarse-grained using the AUTO-MARTINI scheme.<sup>30</sup> AUTO-MARTINI automatically determines the coarse-grained force field in two steps: (i) the CG mapping is optimized according to Martini-based heuristic rules and (ii) interactions are set by determining a type for each bead, selected from chemical properties of the encapsulated atoms, especially water/octanol partitioning, net charge, and hydrogen-bonding.

### ACKNOWLEDGEMENTS

The authors thank Clemens Rauer, Kurt Kremer, and Omar Valsson for critical reading of the manuscript. The authors acknowledge Chemaxon for providing them with an academic research license for the Marvin Suite. This work was supported by the Emmy Noether program of the Deutsche Forschungsgemeinschaft (DFG). The authors gratefully acknowledge the computing time granted by the John von Neumann Institute for Computing (NIC) and provided on the supercomputer JURECA at Jülich Supercomputing Centre (JSC).

### SUPPORTING INFORMATION

In the supporting information (SI) we describe (i) our modeling of the inhomogeneous diffusivity,  $D(z)$ , and provide a sensitivity analysis; (ii) the representation of a (de)protonation reaction at the coarse-grained level; (iii) separate permeability surfaces for unimers and dimers; (iv) an extension to zwitterionic compounds; (v) validation of the CG simulations against both atomistic simulations and experiments (vi) a validation of the predictions extracted from the permeability surface against coarse-grained and atomistic simulations; and (vii) detailed statistics of the functional group populations corresponding to blue regions in fig. 3.

<sup>1</sup> C. A. Lipinski, F. Lombardo, B. W. Dominy, and P. J. Feeney, *Advanced drug delivery reviews* **46**, 3 (2001).

<sup>2</sup> Y. J. Colón and R. Q. Snurr, *Chemical Society Reviews* **43**, 5735 (2014).

- <sup>3</sup> L. Di and E. H. Kerns, *Drug-like properties: concepts, structure design and methods from ADME to toxicity optimization* (Academic press, 2015).
- <sup>4</sup> T. Bereau, D. Andrienko, and K. Kremer, *APL Materials* **4**, 6391 (2016).
- <sup>5</sup> R. Menichetti, K. H. Kanekal, K. Kremer, and T. Bereau, *The Journal of Chemical Physics* **147**, 125101 (2017).
- <sup>6</sup> W. M. Pardridge, *Advanced drug delivery reviews* **15**, 5 (1995).
- <sup>7</sup> C. Pidgeon, S. Ong, H. Liu, X. Qiu, M. Pidgeon, A. H. Dantzig, J. Munroe, W. J. Hornback, and J. S. Kasher, *Journal of medicinal chemistry* **38**, 590 (1995).
- <sup>8</sup> M. Yazdaniyan, S. L. Glynn, J. L. Wright, and A. Hawi, *Pharmaceutical research* **15**, 1490 (1998).
- <sup>9</sup> T. R. Stouch, J. R. Kenyon, S. R. Johnson, X.-Q. Chen, A. Doweyko, and Y. Li, *Journal of computer-aided molecular design* **17**, 83 (2003).
- <sup>10</sup> R. V. Swift and R. E. Amaro, *Chemical biology & drug design* **81**, 61 (2013).
- <sup>11</sup> L. Zhang, J. Tan, D. Han, and H. Zhu, *Drug discovery today* **22**, 1680 (2017).
- <sup>12</sup> C. M. Dobson, *Nature* **432**, 824 (2004).
- <sup>13</sup> D. R. Spring, *Organic & biomolecular chemistry* **1**, 3867 (2003).
- <sup>14</sup> M. Orsi and J. W. Essex, *Molecular Simulations and Biomembranes*, 76 (2010).
- <sup>15</sup> J. M. Diamond and Y. Katz, *J. Membrane Biol.* **17**, 121 (1974).
- <sup>16</sup> S.-J. Marrink and H. J. Berendsen, *J. Phys. Chem.* **98**, 4155 (1994).
- <sup>17</sup> L. W. Votapka, C. T. Lee, and R. E. Amaro, *The Journal of Physical Chemistry B* **120**, 8606 (2016).
- <sup>18</sup> T. S. Carpenter, D. A. Kirshner, E. Y. Lau, S. E. Wong, J. P. Nilmeier, and F. C. Lightstone, *Biophys. J.* **107**, 630 (2014).
- <sup>19</sup> C. T. Lee, J. Comer, C. Herndon, N. Leung, A. Pavlova, R. V. Swift, C. Tung, C. N. Rowley, R. E. Amaro, C. Chipot, Y. Wang, and J. C. Gumbard, *Journal of chemical information and modeling* **56**, 721 (2016).
- <sup>20</sup> B. J. Bennion, N. A. Be, M. W. McNERney, V. Lao, E. M. Carlson, C. A. Valdez, M. A. Malfatti, H. A. Enright, T. H. Nguyen, F. C. Lightstone, and T. S. Carpenter, *The Journal of Physical Chemistry B* **121**, 5228 (2017).
- <sup>21</sup> C. H. Tse, J. Comer, Y. Wang, and C. Chipot, *Journal of chemical theory and computation* **14**, 2895 (2018).
- <sup>22</sup> L. M. Ghiringhelli, J. Vybiral, S. V. Levchenko, C. Draxl, and M. Scheffler, *Physical review letters* **114**, 105503 (2015).
- <sup>23</sup> O. Isayev, C. Oses, C. Toher, E. Gossett, S. Curtarolo, and A. Tropsha, *Nature communications* **8**, 15679 (2017).
- <sup>24</sup> W. G. Noid, *J. Chem. Phys.* **139**, 090901 (2013).
- <sup>25</sup> G. A. Voth, *Coarse-graining of condensed phase and biomolecular systems* (CRC press: Boca Raton, FL, 2008).
- <sup>26</sup> S. J. Marrink, A. H. de Vries, and A. E. Mark, *J. Phys. Chem. B* **108**, 750 (2004).
- <sup>27</sup> S. J. Marrink, H. J. Risselada, S. Yefimov, D. P. Tieleman, and A. H. de Vries, *J. Phys. Chem. B* **111**, 7812 (2007).
- <sup>28</sup> S. J. Marrink and D. P. Tieleman, *Chemical Society Reviews* **42**, 6801 (2013).
- <sup>29</sup> R. Menichetti, K. Kremer, and T. Bereau, *Biochemical and biophysical research communications* **498**, 282 (2018).
- <sup>30</sup> T. Bereau and K. Kremer, *J. Chem. Theory Comput.* **11**, 2783 (2015).
- <sup>31</sup> J. L. MacCallum, W. D. Bennett, and D. P. Tieleman, *Biophys. J.* **94**, 3393 (2008).
- <sup>32</sup> "Calculator Plugin of ChemAxon Marvin 17.28.0," (2017).
- <sup>33</sup> T. Fink, H. Bruggesser, and J.-L. Reymond, *Angewandte Chemie International Edition* **44**, 1504 (2005).
- <sup>34</sup> T. Fink and J.-l. Reymond, *J. Chem. Inf. Model.* **47**, 342 (2007).
- <sup>35</sup> P. Bruice, *Organic Chemistry*, Always Learning (Pearson, 2016).
- <sup>36</sup> I. V. Tetko and V. Y. Tanchuk, *J. Chem. Inf. Comput. Sci.* **42**, 1136 (2002).
- <sup>37</sup> G. Lambrinidis, F. Tsopelas, C. Giaginis, and A. Tsantili-Kakoulidou, "Qsar/qspr modeling in the design of drug candidates with balanced pharmacodynamic and pharmacokinetic properties," in *Advances in QSAR Modeling: Applications in Pharmaceutical, Chemical, Food, Agricultural and Environmental Sciences*, edited by K. Roy (Springer International Publishing, Cham, 2017) pp. 339–384.
- <sup>38</sup> N.-N. Wang, J. Dong, Y.-H. Deng, M.-F. Zhu, M. Wen, Z.-J. Yao, A.-P. Lu, J.-B. Wang, and D.-S. Cao, *Journal of Chemical Information and Modeling* **56**, 763 (2016).
- <sup>39</sup> A. P. Bento, A. Gaulton, A. Hersey, L. J. Bellis, J. Chambers, M. Davies, F. A. Krüger, Y. Light, L. Mak, S. McGlinchey, M. Nowotka, G. Papadatos, R. Santos, and J. P. Overington, *Nucleic acids research* **42**, D1083 (2014).
- <sup>40</sup> C. Ballatore, D. M. Huryn, and A. B. Smith, *ChemMedChem* **8**, 385 (2013).
- <sup>41</sup> A. Dahan, A. Beig, D. Lindley, and J. M. Miller, *Advanced drug delivery reviews* **101**, 99 (2016).
- <sup>42</sup> F. A. Faber, A. Lindmaa, O. A. Von Lilienfeld, and R. Armiento, *Physical review letters* **117**, 135502 (2016).
- <sup>43</sup> A. P. Bartók, S. De, C. Poelking, N. Bernstein, J. R. Kermode, G. Csányi, and M. Ceriotti, *Science advances* **3**, e1701816 (2017).
- <sup>44</sup> B. Hess, C. Kutzner, D. Van Der Spoel, and E. Lindahl, *J. Chem. Theory Comput.* **4**, 435 (2008).
- <sup>45</sup> D. H. De Jong, S. Baoukina, H. I. Ingólfsson, and S. J. Marrink, *Comput. Phys. Commun.* **199**, 1 (2016).
- <sup>46</sup> M. Parrinello and A. Rahman, *J. Appl. Phys.* **52**, 7182 (1981).
- <sup>47</sup> G. Bussi, D. Donadio, and M. Parrinello, *J. Chem. Phys.* **126**, 014101 (2007).
- <sup>48</sup> T. A. Wassenaar, H. I. Ingólfsson, R. A. Böckmann, D. P. Tieleman, and S. J. Marrink, *J. Chem. Theory Comput.* **11**, 2144 (2015).
- <sup>49</sup> G. M. Torrie and J. P. Valleau, *J. Comput. Phys.* **23**, 187 (1977).
- <sup>50</sup> T. Bereau, Z.-J. Wang, and M. Deserno, *J. Chem. Phys.* **140**, 03B615-1 (2014).
- <sup>51</sup> S. Kumar, J. M. Rosenberg, D. Bouzida, R. H. Swendsen, and P. A. Kollman, *J. Comput. Chem.* **13**, 1011 (1992).
- <sup>52</sup> T. Bereau and R. H. Swendsen, *J. Comput. Phys.* **228**, 6119 (2009).
- <sup>53</sup> J. S. Hub, B. L. De Groot, and D. Van Der Spoel, *J. Chem. Theory Comput.* **6**, 3713 (2010).
- <sup>54</sup> J. F. Rudzinski, K. Kremer, and T. Bereau, *The Journal of Chemical Physics* **144**, 051102 (2016).
- <sup>55</sup> C. Liao and M. C. Nicklaus, *Journal of chemical information and modeling* **49**, 2801 (2009).
- <sup>56</sup> N. Haider, *Molecules* **15**, 5079 (2010)

# Supporting Information for “Drug-membrane permeability across chemical space”

Roberto Menichetti, Kiran H. Kanekal, and Tristan Bereau\*  
Max Planck Institute for Polymer Research, 55128 Mainz, Germany

(Dated: December 31, 2018)

## CONTENTS

S1. Introduction	S1
S2. Diffusivity profile	S2
S3. Representing (de)protonation at the CG level	S3
S4. Permeability surfaces: unimers and dimers	S4
S5. Zwitterionic compounds	S4
S6. Comparison of coarse-grained and atomistic simulation results	S5
S7. Permeability surface against coarse-grained/atomistic simulations	S8
S8. Comparison with experimental results	S10
S9. GROMACS input files	S11
S10. Functional Group Distributions	S19
References	S23

## S1. INTRODUCTION

In this Supporting Information we provide additional results integrating those presented in the main text. In Sec. S2 we discuss the inhomogeneous diffusivity profile  $D(z)$  employed in our calculations and test the impact of different choices for this quantity on permeability coefficients. In Sec. S3 we analyze our choice for representing at the CG level the (de)protonated form of a compound. In Sec. S4 we focus on the dependence of the permeability surfaces on molecular weight and analyze results for one- and two-beads CG compounds (“unimers” and “dimers”). In Sec. S5 we extend the discussion about permeability surface and chemical coverage to zwitterionic compounds. In Sec. S6 we compare the permeability coefficient  $P$  of several small molecules obtained via CG molecular dynamics simulations with independent atomistic simulation results. In Sec. S7 we compare the *simulation-free* predictions of permeability coefficients obtained through the permeability surface with coarse-grained and atomistic simulation results. In Sec. S8 we compare CG permeability coefficients  $P$  of several small molecules with independent experimental measurements of their blood-brain-barrier permeability coefficient ( $\log_{10}$  BB). In Sec. S10, we provide detailed statistics about the dominant functional groups present in the highlighted regions of Fig. 3 of the main text.

---

\* bereau@mpip-mainz.mpg.de

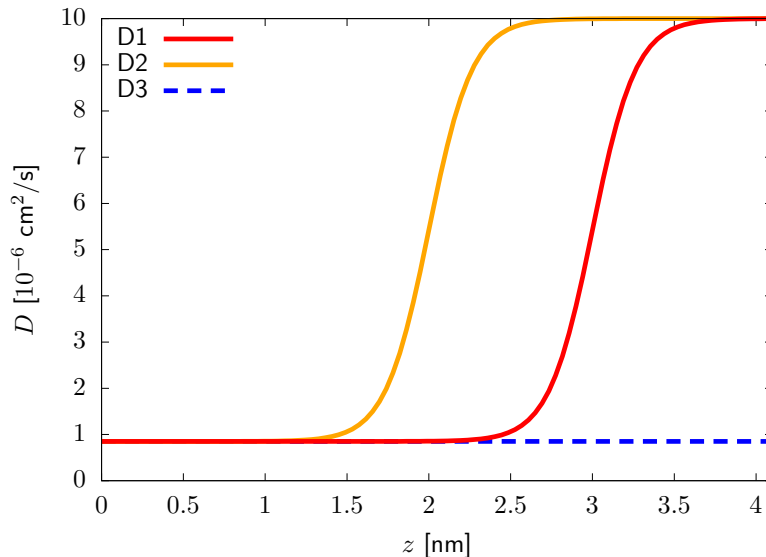


FIG. S1. Local diffusivity employed in this work as a function of the normal distance  $z$  of the compound from the bilayer midplane (D1, red line), together with the alternative profiles introduced to test the sensitivity of permeability coefficients to a change in  $D(z)$  (see Fig. S2): a horizontally shifted version of the final parametrization (D2, orange line) and a uniform profile (D3, blue dashed line).

## S2. DIFFUSIVITY PROFILE

The permeability coefficient  $P$  of a small molecule in a phospholipid bilayer is determined from its potential of mean force  $G(z)$  and inhomogeneous diffusivity  $D(z)$  as [1]

$$P^{-1} = \int dz \frac{\exp[\beta G(z)]}{D(z)}, \quad (\text{S1})$$

with  $\beta = 1/k_B T$ . For compounds with multiple protonation states, both neutral and charged species contribute to the total flux and must be taken into account with a slight modification of Eq. S1 (see Methods in the main text). As the Martini force field is explicitly parametrized to reproduce the thermodynamics of partitioning between solvents of different polarity [2–4], it is capable of providing accurate results for the potential of mean force. On the other hand, the calculation of  $D(z)$  starting from CG molecular dynamics simulations is highly nontrivial due to the tendency of these models to inconsistently accelerate the dynamics [5]. The determination of the inhomogeneous diffusivity of a compound thus still relies on performing expensive atomistic molecular dynamics simulations. However, by comparing the results for several small molecules embedded in a DOPC bilayer it was recently shown that  $D(z)$  is virtually insensitive to the chemical detail [6]. Moreover, from Eq. S1 it is apparent that  $D(z)$  only provides a linear correction to the permeability coefficient, therefore a logarithmic correction to the corresponding order of magnitude ( $\log_{10} P$ ). Starting from these considerations, in the calculation of permeability coefficients we considered a unique effective diffusivity profile across chemical space (and for different protonation states). We parametrized it as

$$D(z) = \alpha + \frac{\beta}{e^{-\gamma(x-\delta)} + 1}, \quad (\text{S2})$$

which correctly captures the main features of its atomistic counterpart, *i.e.*, an increased diffusivity of the compound as it leaves the lipid tails and enters the bulk water environment. We tuned the parameters  $\alpha$ ,  $\beta$ ,  $\gamma$  and  $\delta$  to reproduce the atomistic simulation results of Ref. 6. The final, optimized form of  $D(z)$  employed in our calculations is shown in Fig. S1, with  $\alpha = 0.85 \cdot 10^{-6} \text{ cm}^2/\text{s}$ ,  $\beta = 9.15 \cdot 10^{-6} \text{ cm}^2/\text{s}$ ,  $\gamma = 7.5 \text{ nm}^{-1}$ ,  $\delta = 3 \text{ nm}$ .

We further tested the impact of this quantity on the permeability coefficients—and consequently on the permeability surfaces—by considering two alternative profiles: an horizontally shifted version of the optimized parametrization, and a homogeneous profile. Both curves are shown in Fig. S1. The permeabilities obtained by relying on the three different diffusivities in the case of neutral compounds are presented in Fig. S2 as a function of the water/membrane

partitioning free energy  $\Delta G_{W \rightarrow M}$ . It is apparent that a change in  $D(z)$  only affects the permeability of hydrophobic

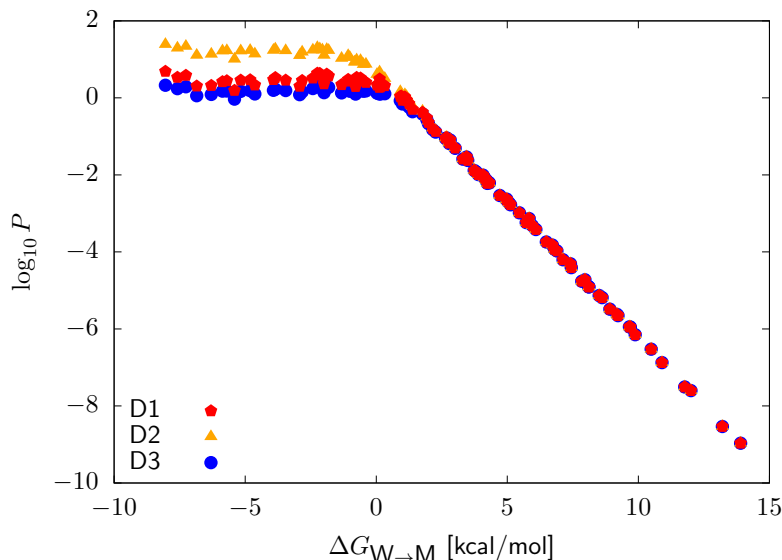


FIG. S2. Permeability coefficient ( $\log_{10}$  scale) of a neutral compound as a function of its water/membrane free energy  $\Delta G_{W \rightarrow M}$  obtained by considering the three different diffusivities  $D(z)$  shown in Fig. S1: the optimized parametrization (D1), its horizontally shifted version (D2), and a homogeneous profile (D3). Key labels and colors coding follow those of Fig. S1.

compounds ( $\Delta G_{W \rightarrow M} \lesssim 0$ ). Most importantly, deviations are within one  $\log_{10}$  unit, which is our degree of accuracy in predicting permeability coefficients. These results are in agreement with previous studies that correlated a variation of one order of magnitude in the inhomogeneous diffusivity to roughly one  $\log_{10}$  unit in the permeability coefficient [7].

### S3. REPRESENTING (DE)PROTONATION AT THE CG LEVEL

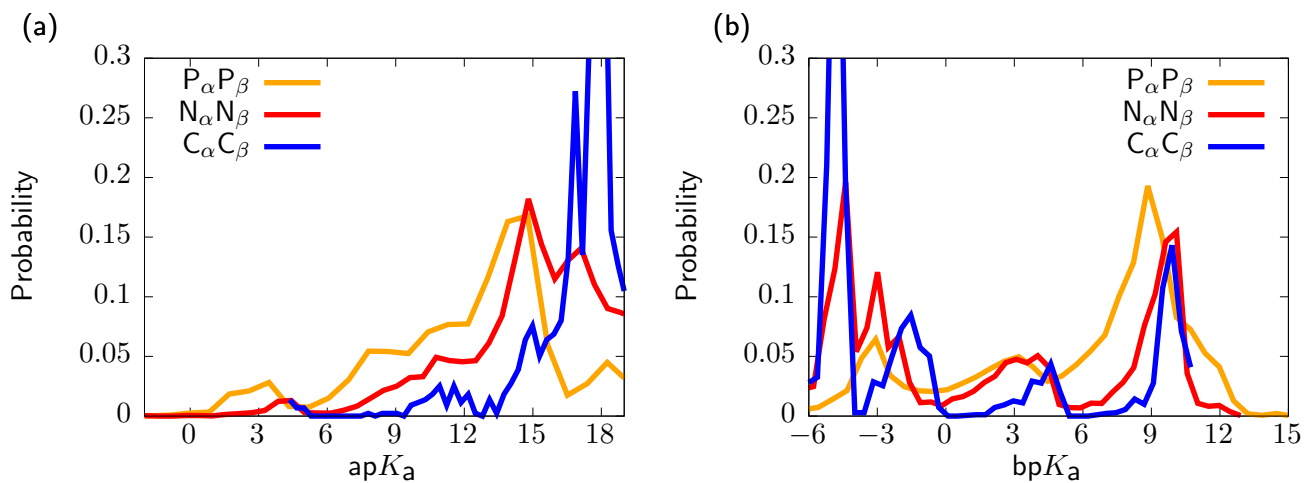


FIG. S3.  $apK_a$  (a) and  $bpK_a$  (b) histograms for all compounds in the GDB database mapping to coarse-grained dimers that only contain a combination of beads with the same degree of polarity: Polar ( $P_\alpha P_\beta$ ), nonpolar ( $N_\alpha N_\beta$ ) and apolar ( $C_\alpha C_\beta$ ) compounds—following the standard Martini notation [2–4].

The Martini mapping of a small molecule is obtained by decomposing it in chemical fragments and associating a

bead type appropriately selected from the Martini list to each fragment [8]. As in the calculation of the permeability coefficient one has to account for the different protonation states of a compound (see Methods section in the main text), it is necessary to discuss how to represent (de)protonation reactions at the coarse-grained level: in other words, how to determine the Martini parametrization of the (de)protonated form of a compound starting from the neutral case. In the following, we will focus on the set of coarse-grained molecules considered in this work, *i.e.*, unimers and dimers.

Within a neutral compound, (de)protonating a chemical group leaves the corresponding chemical fragment with a (negative) positive charge. Therefore, at the coarse-grained level the neutral bead encapsulating the fragment has to be accordingly replaced with a charged one. In Martini, the charged bead can be selected among four different types, mimicking different hydrogen-bond capabilities:  $Q_0$  (no hydrogen bond),  $Q_{da}$  (donor/acceptor),  $Q_a$  (acceptor) or  $Q_d$  (donor) [2–4].

We systematically represent the protonated form of a chemical fragment by means of a positively charged donor bead type ( $Q_{d,+1}$ ), while the deprotonated form with a negatively charged acceptor bead type ( $Q_{a,-1}$ ). Although (de)protonation could allow the fragment to have both hydrogen-bond donor *and* acceptor capabilities, employing a  $Q_{da}$  bead type does not significantly impact the resulting permeability coefficients.

While for small molecules that map to unimers the charged bead type uniquely determines the coarse-grained representation of their (de)protonated form, in the case of dimers there is an additional degree of freedom associated to the choice of the site. Indeed, starting from a neutral dimer  $B_1B_2$  there are two different possibilities depending on which chemical fragment is subject to (de)protonation:  $Q_1B_2$  and  $B_1Q_2$ . Rather than considering all possible cross-combinations of neutral and charged bead types, in the case of dimers we employ a data-driven approach to estimate the bead type most likely to (de)protonate. We thus extracted from the GDB database all compounds mapping to polar (combination of  $P_\alpha P_\beta$  bead types, following the standard Martini notation [2–4]) nonpolar ( $N_\alpha N_\beta$ ) and apolar ( $C_\alpha C_\beta$ ) dimers, and separately calculated  $apK_a$  and  $bpK_a$  histograms in the three cases. The resulting distributions shown in Fig. S3 suggest a correlation between the polarity of the Martini bead type and the acid/base strength of the encapsulated chemical fragment. Strongest acids/bases tend to be represented by polar beads  $P_\alpha$ , followed by non-polar  $N_\alpha$  and apolar  $C_\alpha$  ones. Starting from these results, in the case of dimers we assumed that (de)protonation always occurs within the chemical fragment represented by the more polar bead type.

We relied on this set of assumptions for the calculation of permeability surfaces (Fig. S4 and Fig. 2 in the main text) and in the databases of permeability coefficients for the 510,000 small molecules extracted from the GDB database.

#### S4. PERMEABILITY SURFACES: UNIMERS AND DIMERS

We discuss how the permeability surfaces (main text, Fig. 2) depend on molecular weight. At the CG level, this corresponds to an increase in the number of beads of the small molecule. For both unimers to dimers, Fig. S4 displays permeability surfaces as a function of the acidic or basic  $pK_a$  of the compound in water ( $apK_a$  and  $bpK_a$ ) and its water/membrane partitioning free energy  $\Delta G_{W \rightarrow M}$ .

In analogy with what we observe in the case of chemical coverage (see Fig. 3 in the main text), going from unimers to dimers broadens the range of water/membrane partitioning free-energies. This stems from the extensive nature of the partitioning coefficient. On the other hand, a comparison of the surfaces in the range  $-4 \lesssim \Delta G_{W \rightarrow M} \lesssim 7$  [kcal/mol]—separately for panels (a,c) and (b,d)—highlights the extremely good transferability of the results across molecular weights, as the profiles corresponding to unimers and dimers superimpose to a large extent.

#### S5. ZWITTERIONIC COMPOUNDS

We now extend the discussion about permeability surface and chemical coverage (Figs. 2,3 in the main text) to zwitterionic compounds, which consist of two acid/base reactions while keeping the molecule electrically neutral.

In analogy to the case of compounds presenting a single (de)protonation reaction, both the neutral and doubly-charged species contribute to the permeability coefficient through the total resistivity (see Eq. 2 in the main text). The corresponding potentials of mean force  $G_N(z)$  and  $G_C(z)$  must be offset by the free-energy difference between the neutral compound and the zwitterionic form in bulk water. By assuming independence of the individual reactions, this offset can be written as

$$G_{\text{neut}} = G_{\text{zwit}} + k_B T (\text{bp}K_a - \text{ap}K_a) \ln 10, \quad (\text{S3})$$

which depends on the *difference* in ionization species,  $\text{bp}K_a - \text{ap}K_a$ . We require that the zwitterionic form is more stable than both the neutral and single-charged species, leading to the additional constraint  $\text{bp}K_a \gtrsim 7.4$  and

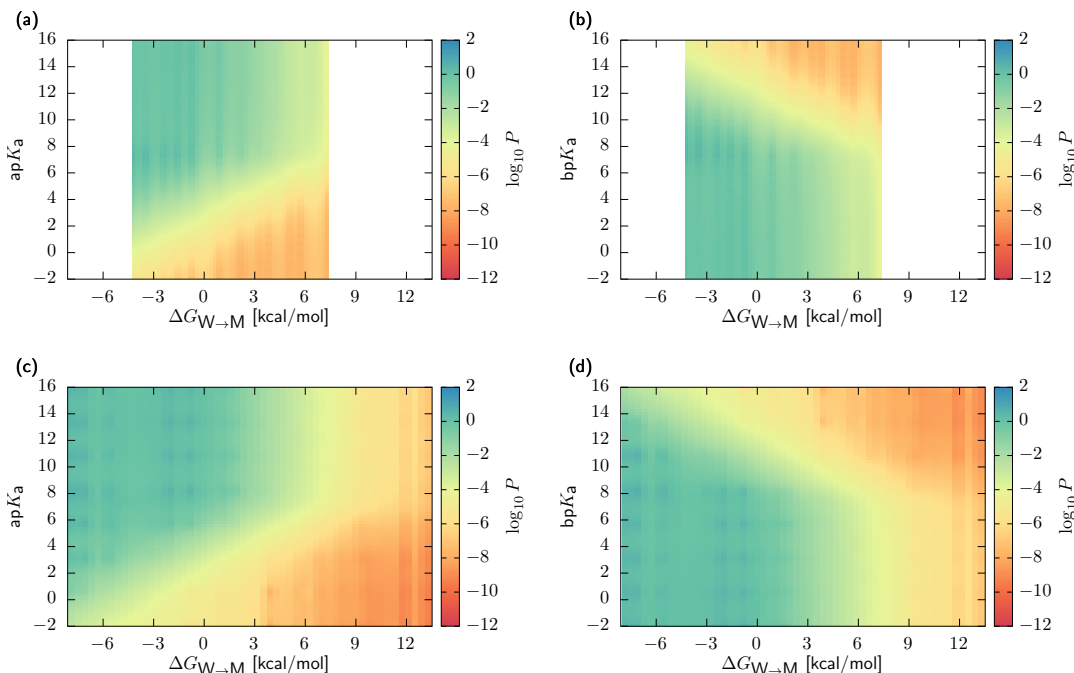


FIG. S4. Permeability surfaces ( $\log_{10}$  scale) for Martini unimers (a,b) and dimers (c,d) as a function of two small-molecule descriptors: the acidic or basic  $pK_a$  in water and the water/membrane partitioning free energy. We employ a common range in the horizontal axis for unimers and dimers in order to underline the transferability of the surfaces across molecular weights (see text). Cooler (warmer) colors correspond to faster (slower) permeating molecules.

$apK_a \lesssim 7.4$ .

As in the case of acidic and basic compounds (see Sec. S3), it is necessary to discuss how to represent the zwitterionic form of a compound at the coarse-grained level. We again distinguish between unimers and dimers.

In unimers, the protonation and deprotonation reactions occur within the same chemical fragment, so that the coarse-grained representation of the doubly-charged form of a compound coincides with the original, neutral one. The minimum length scale accessible by the coarse-grained model (roughly of the size of the chemical fragment) thus precludes to represent a zwitterionic compound in terms of a single bead.

In the case of dimers, we assumed that the protonation and deprotonation reactions occur in chemical fragments belonging to two different beads, thus leading to a CG compound containing two opposite charges starting from the neutral one. Together with our choice of the bead types for representing (de)protonated chemical fragments (see Sec. S3), this means that given a neutral  $B_1 B_2$  dimer its zwitterionic form is  $Q_{a,-1} Q_{d,+1}$ .

We relied on these assumptions to calculate the permeability surface for zwitterionic compounds that map to coarse-grained dimers. Results are shown in Fig. S5a. Akin to the single-protonation compounds (Fig. S4), the surface shows a strong dependence on both descriptors ( $bpK_a - apK_a$  and  $\Delta G_{W \rightarrow M}$ ) with hydrophobic compounds generally leading to larger permeability coefficients. These also require smaller values of  $bpK_a - apK_a$ , i.e., weaker acids and bases. Stronger acid/base compounds significantly lower the permeability coefficient, reaching values often lower than for the single-protonation cases (Fig. S4).

The corresponding chemical-space coverage is shown in Fig. S5b. Unsurprisingly, it displays many functional groups that are present in *both*  $apK_a$  and  $bpK_a$  coverages (Fig. 3 in the main text). Notable examples are carboxylic groups as well as certain aromatic heterocyclic compounds.

## S6. COMPARISON OF COARSE-GRAINED AND ATOMISTIC SIMULATION RESULTS

In this work, we determined permeability coefficients through Eq. S1 by considering a unique effective diffusivity profile across chemical space (see Sec. S2), combining it with potentials of mean force  $G(z)$  extracted from CG simulations. In order to assess the accuracy of these results, we now test them against independent atomistic simulation

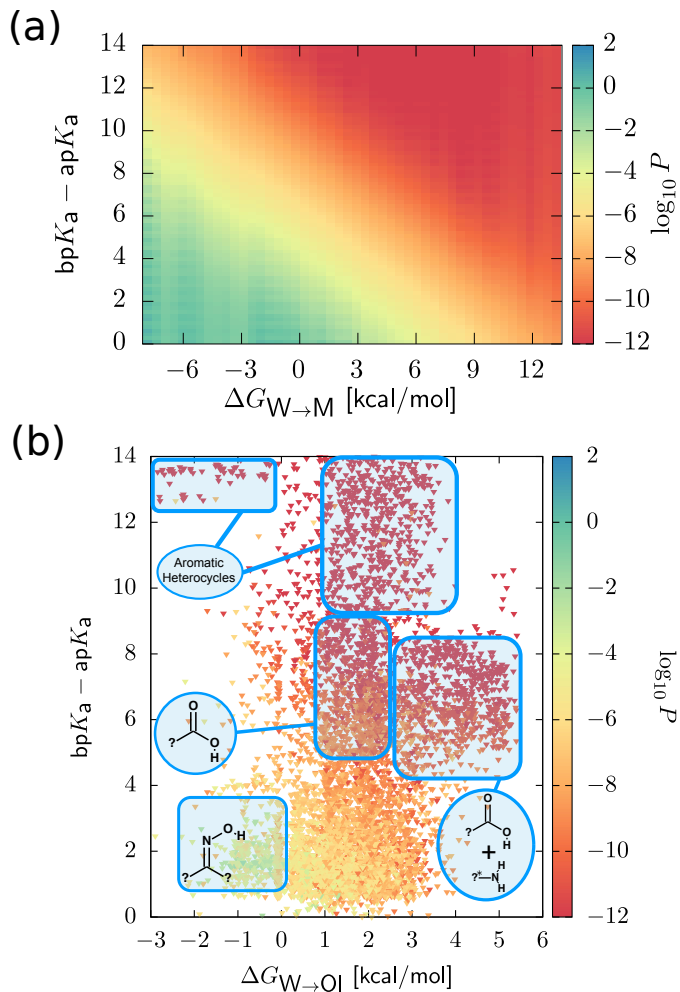


FIG. S5. (a) Permeability surface of zwitterionic compounds. Captions follow of those of Fig. S4. (b) Chemical-space coverage of GDB zwitterions projected onto  $pK_a$  and water/octanol partitioning free energies  $\Delta G_{W \rightarrow O1}$ . Regions highlighted in light blue display several representative chemical groups. Substitutions denoted by “?” correspond to H, alkyl, or aryl groups, while “?\*” only correspond to alkyl groups.

ones [6, 7].

Having employed a unique diffusivity profile in our calculations, it is necessary to first discuss the sensitivity of atomistic permeability coefficients with respect to a replacement of the original diffusivity  $D(z)$  of a compound with our effective profile. We performed this analysis on a subset of the compounds that in Ref. 6, 7 were investigated by means of atomistic simulations, excluding from the calculations all molecules containing multiple intertwined rings due to difficulties in obtaining their coarse-grained representation. It is important to stress that the compounds investigated in Ref. 7 were embedded in a dimyristoylphosphatidylcholine (DMPC) bilayer, a different lipid with respect to the one considered in this work (DOPC). In the case of Urea and Benzoic (“Ur” and “Benz” in the inset of Fig. S6), this required us to slightly modify the effective diffusivity profile to account for the difference in membrane composition.

For the set of compounds considered, in the inset of Fig. S6 and in Table S1 we compare the atomistic permeability coefficients  $\log_{10} \bar{P}_{AA}$  reported in Ref. 6, 7 with the  $\log_{10} P_{AA}$  we obtained by means of our effective diffusivity—*i.e.*, calculated by means of the atomistic  $G(z)$  and the profile presented in Fig. S1. The excellent correlation between these two quantities confirms that the introduction of the effective diffusivity doesn’t significantly impact the permeability coefficient, which largely depend on the potential of mean force  $G(z)$ . In the case of Urea [7] (“Ur” in Fig. S6), the only statistically significant outlier, the observed discrepancy is due to difficulties to visually extract the atomistic  $D(z)$  close to the bilayer midplane  $z \approx 0$  in Ref. 7.

We now compare atomistic and coarse-grained simulation predictions for permeability coefficients to assess the

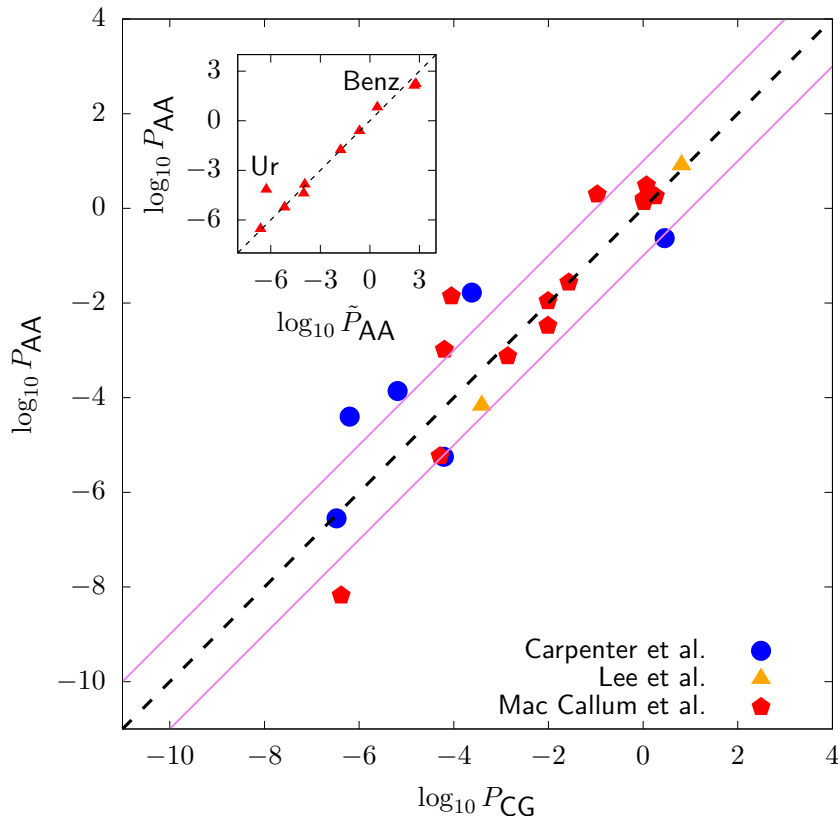


FIG. S6. Inset: Correlation between permeability coefficients  $\log_{10} \tilde{P}_{AA}$  calculated from AA simulations [6, 7], and the  $\log_{10} P_{AA}$  obtained by combining AA potentials of mean force  $G(z)$  with the effective diffusivity profile  $D(z)$  presented in Fig. S1. Urea and Benzoic acid—see text—are marked with the labels “Ur”, “Benz”. Main: Correlation between permeability coefficient calculated via AA and CG potentials of mean force ( $\log_{10} P_{AA}$  and  $\log_{10} P_{CG}$ , respectively), in both cases relying on the effective diffusivity profile presented in Fig. S1. We present results for the compound extracted from Ref. 6 (“Carpenter et al.”), Ref. 7 (“Lee et al.”) and Ref. 9 (“Mac Callum et al.”).

accuracy of the latter. As atomistic reference data, we first considered the previously introduced set of compounds extracted from Refs. 6, 7. We systematically coarse-grained all these compounds through the AUTO-MARTINI tool [8], again excluding from the calculations all chemical compounds containing multiple intertwined rings. In the case of atenolol and salbutamol, we had to account for the presence of discrepancies in the ALOGPS [10] prediction of water/octanol partitioning free energy against experimental measurements for specific chemical fragments by slightly fine-tuning the AUTO-MARTINI output. For completeness, in Sec. S9 we report GROMACS input files with the final force-field parametrization for the entire set of small molecules. Subsequently, we performed CG molecular dynamics simulations as described in the Methods section of the main text and calculated the corresponding CG permeability coefficients  $\log_{10} P_{CG}$ .

Given that the set contains only a limited number of compounds—most of them being beyond the upper limit in molecular weight considered in this work—we further included in the analysis the subset of amino-acid side chains discussed in Ref. 11, whose behavior in a DOPC membrane was analyzed in Ref. 9 by means of atomistic simulations. Unfortunately, Ref. 9 doesn’t provide results for the atomistic diffusivity  $D(z)$ . However, having established that the use of the effective diffusivity provides consistent permeability coefficients within the degree of accuracy pursued in this work (inset of Fig. S6), we employed this profile together with the atomistic  $G(z)$  to determine the permeability coefficients  $\log_{10} P_{AA}$  of amino-acid side chains. The corresponding coarse-grained  $\log_{10} P_{CG}$  were again determined by means of CG simulations.

A comparison between permeability coefficients obtained by means of atomistic and coarse-grained simulations ( $\log_{10} P_{AA}$  and  $\log_{10} P_{CG}$ , respectively) for all 21 compounds is presented in Fig. S6 and Table S1. For consistency among atomistic results, the  $\log_{10} P_{AA}$  of all compounds are calculated by considering the atomistic potential of mean

force  $G(z)$ , together with the effective diffusivity profile. Overall, Fig. S6 suggests a high correlation between atomistic and CG results, which extends over a wide range of orders of magnitude and beyond the range of molecular weights investigated in this work—Pearson correlation coefficient  $R^2 \approx 0.9$ , with a mean absolute error of roughly one  $\log_{10}$  unit—thus confirming the accuracy of CG models in predicting the permeability coefficient of a compound.

### S7. PERMEABILITY SURFACE AGAINST COARSE-GRAINED/ATOMISTIC SIMULATIONS

The surfaces presented in Fig. S4, S5 and Fig. 2 of the main text enable the calculation of the permeability coefficient of a compound only starting from two key molecular properties: the water/octanol partitioning free energy  $\Delta G_{W \rightarrow O1}$  and acid dissociation constant  $pK_a$ . We now validate these *simulation-free* predictions against the ones obtained by performing explicit simulations, either atomistic or coarse-grained, again considering the 21 chemical compounds introduced in Sec. S6.

As the permeability surfaces were derived for all compounds ranging from 30 to 160 Da that map to coarse-grained unimers and dimers, we accordingly distinguish between the small molecules that satisfy both these constraints (set M1) and the ones who don't (set M2). While M1 will allow for a direct validation of the permeabilities obtained from the surface, M2 will give insights into the transferability of our results across molecular weight and coarse-grained representations.

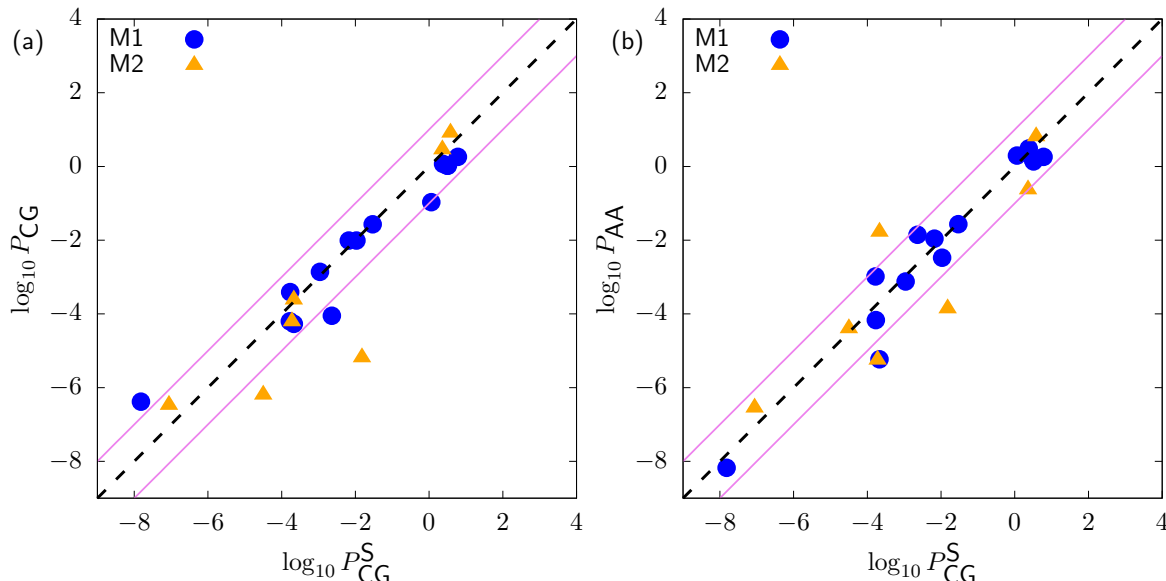


FIG. S7. Comparison of the *simulation-free* permeability coefficients  $\log_{10} P_{CG}^S$  extrapolated from the permeability surface with coarse-grained  $\log_{10} P_{CG}$  (a) and atomistic  $\log_{10} P_{AA}$  (b) simulation results, both calculated relying on the effective diffusivity profile. We present results for small molecules extracted from Refs. 6, 7, 9, dividing them according to whether they are within (M1) or outside (M2) the range of molecular weights (30 – 160 Da) and coarse-grained representations (unimers and dimers) investigated in this work.

For each of the 21 compounds, we first determined the molecular water/octanol partitioning free-energy and  $pK_a$  by means on the ALOGPS [10] and CHEMAXON MARVIN [12] prediction tools. Calculating a permeability coefficient from the surface requires to convert  $\Delta G_{W \rightarrow O1}$  into the water/membrane partitioning free energy  $\Delta G_{W \rightarrow M}$ : this can be done by relying on the linear relations presented in Ref. 11. These relations are molecular-weight dependent, and in Ref. 11 were determined for all small molecules in the range 30 – 160 Da that map onto coarse-grained unimers and dimers. For the 14 compounds belonging to the set M1, this allowed us to directly calculate their  $\Delta G_{W \rightarrow M}$  starting from  $\Delta G_{W \rightarrow O1}$ .

In the set M2, salicylate and benzoic acid are within the correct range of molecular weight but present a different coarse-grained representation (four beads due to the presence of an aromatic ring). Mannitol has a slightly larger molecular weight (182 Da), and maps onto a coarse-grained dimer. Atenolol, cimetidine, ibuprofen and salbutamol present both molecular weights higher than 160 Da and different coarse-grained representations. As the water/octanol to water/membrane relationship is unknown in these cases, we calculated their  $\Delta G_{W \rightarrow M}$  from  $\Delta G_{W \rightarrow O1}$  by relying

	$\log_{10} \tilde{P}_{AA}$	$\log_{10} P_{AA}$	$\log_{10} P_{CG}$	$\log_{10} P_{CG}^S$
Atenolol	-1.77	-1.78	-3.62	-3.67
Cimetidine	-3.94	-3.86	-5.19	-1.82
Ibuprofen	-0.63	-0.63	0.45	0.36
Mannitol	-6.62	-6.55	-6.48	-7.06
Salbutamol	-4	-4.40	-6.20	-4.50
Salicylate	-5.17	-5.25	-4.21	-3.72
Urea	-6.27	-4.17	-3.41	-3.77
Benzoic acid	0.45	0.81	0.91	0.58
ser	—	-1.96	-2.01	-2.18
cys	—	0.29	-0.97	0.06
met	—	0.26	0.26	0.78
thr	—	-1.56	-1.57	-1.53
asn	—	-3.12	-2.86	-2.96
val	—	0.14	0.02	0.51
leu	—	0.20	0.02	0.49
ile	—	0.49	0.07	0.38
gln	—	-2.48	-2.01	-1.97
arg	—	-8.17	-6.38	-7.82
asp	—	-2.98	-4.20	-3.78
glu	—	-5.23	-4.27	-3.67
lys	—	-1.85	-4.05	-2.64

TABLE S1. Permeability coefficients ( $\log_{10}$  scale) calculated for the validation set of 21 compounds analyzed in this work. We report atomistic simulation results [6, 7] ( $\log_{10} \tilde{P}_{AA}$ ), atomistic ( $\log_{10} P_{AA}$ ) and coarse-grained ( $\log_{10} P_{CG}$ ) simulation results calculated by relying on the effective diffusivity profile, and *simulation-free* predictions  $\log_{10} P_{CG}^S$  extrapolated from the permeability surface.

on the one appropriate for coarse-grained dimers.

A projection of the calculated  $\Delta G_{W \rightarrow M}$  and  $pK_a$  of each small molecule on the corresponding surface allowed us to estimate its permeability coefficient  $\log_{10} P_{CG}^S$ . Results for all 21 compounds are presented in Table S1. Furthermore, in Fig. S7a,b we separately compare the extrapolated  $\log_{10} P_{CG}^S$  with the permeabilities obtained by means of coarse-grained ( $\log_{10} P_{CG}$ ) and atomistic ( $\log_{10} P_{AA}$ ) simulations, in both cases calculated by relying on the effective diffusivity profile.

Fig. S7a shows that for all compounds belonging to the set M1 the *simulation-free* prediction of the permeability coefficient is in good agreement with the one calculated via explicit coarse-grained simulations (restricted to M1, we have  $R^2 \approx 0.92$  with a mean absolute error of 1  $\log_{10}$  unit). Therefore, an a posteriori extrapolation from the permeability surface has a negligible effect on the coarse-grained results.

Within the set M2, molecules slightly above the range of molecular weights investigated in this work are characterized by level of accuracy that is comparable to the one of the set M1. However, further increasing the molecular weight (and coarse-grained representations) of the compound concurrently generates an increase in the deviation between extrapolated and coarse-grained permeabilities. Going from mannitol (182 Da) to salbutamol and cimetidine (239 and 252 Da, respectively), the discrepancy between the two predictions grows from 0.4 up to roughly 3  $\log_{10}$  units. This is a consequence of approximating the unknown  $\Delta G_{W \rightarrow M}$  to  $\Delta G_{W \rightarrow OI}$  relation in the case of high molecular-weight molecules with the one appropriate to describe smaller ones. In all cases, the molecular-weight-dependent mapping from water/octanol to water/membrane thus limits the transferability of our predictions [11].

Interestingly, the  $\log_{10} P_{CG}^S$  predictions for urea and benzoic acid extracted from the surface characteristic of the DOPC bilayer are in good agreement with the  $\log_{10} P_{CG}$  obtained by directly simulating a DMPC membrane.

In Fig. S7b we further compare the permeability coefficients  $\log_{10} P_{CG}^S$  extrapolated from the surface with the corresponding  $\log_{10} P_{CG}$  obtained by means of atomistic simulations. Overall, the accuracy is similar to the one associated to coarse-grained simulations (Fig. S6)— $R^2 \approx 0.9$ , with a mean absolute error of 1  $\log_{10}$  unit.

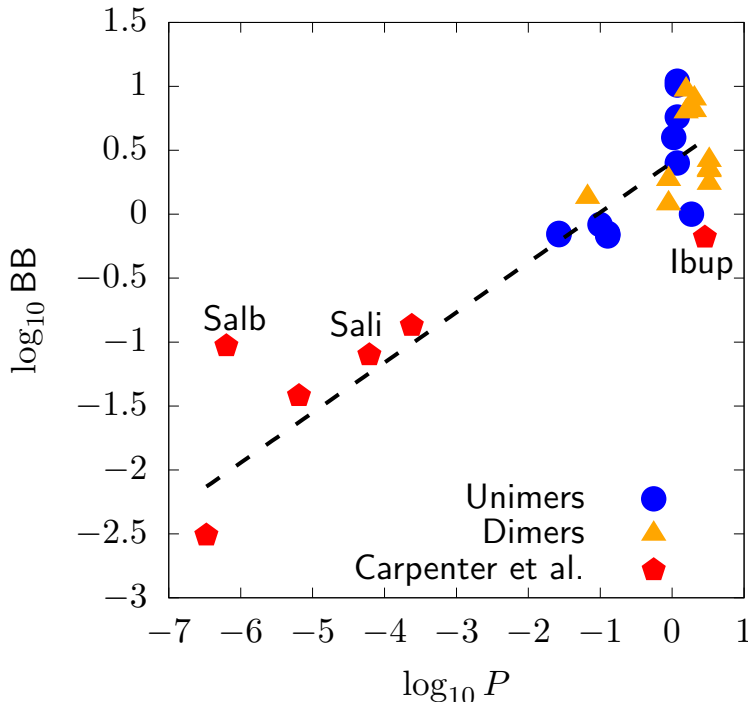


FIG. S8. Correlation between permeability coefficients ( $\log_{10}$  scale) calculated from CG simulations and experimental blood-brain-barrier permeability coefficients  $\log_{10}$  BB. We present results for small molecules extracted from the database of experimental  $\log_{10}$  BB reported in Ref. 13, dividing them according to their CG representation: unimers (blue circles) and dimers (orange triangles). We further present calculations for a subset of the compounds analyzed in Ref. 6 (red pentagons). Salicylate and ibuprofen, explicitly discussed in the main text, are marked with the labels “Sali” and “Ibu”. Salbutamol, the only statistically significant outlier—see text—is marked with the label “Salb”.

## S8. COMPARISON WITH EXPERIMENTAL RESULTS

The permeation rates calculated for several chemically different compounds through Eq. S1 and atomistic molecular dynamics simulations were shown to exhibit extremely high correlations with their experimental counterparts, *e.g.*, blood-brain-barrier ( $\log_{10}$  BB) or PAMPA permeability coefficients [6, 14]. It is therefore important to perform the same analysis on the results we obtain by employing CG models.

We first considered the dataset of experimental  $\log_{10}$  BB permeabilities provided in Ref. 13 to test the accuracy of our results in the range of molecular weights investigated in this work (30 – 160 Da). We systematically coarse-grained all the compounds contained therein by means of the AUTO-MARTINI tool [8], and extracted those whose CG representation consists of one and two beads. This set contains the small alcohols (*e.g.*, propanol and butanol) and the fully-unsubstituted hydrocarbons discussed in the enhanced molecular design section of the main text. A correlation plot of the  $\log_{10}$   $P$  predicted by coarse-grained simulations with their experimental  $\log_{10}$  BB counterparts is presented in Fig. S8.

Given the limited range in  $\log_{10}$  BB covered by this database, we further decided to include the subset of the small molecules already discussed in Sec. S6, which in Ref. 6 were analyzed by means of atomistic molecular dynamics simulations. Overall, the permeability coefficients extracted from CG simulations exhibit a high correlation— $R^2 \approx 0.84$ , with a mean absolute error of one  $\log_{10}$  unit in the permeability coefficient—with experimental  $\log_{10}$  BB measurements over a wide range of orders of magnitude.

In the case of chemical compounds mapping to Martini unimers and dimers, we highlight the presence of sequence of data points at constant  $\log_{10}$   $P$ , spanning an interval of one  $\log_{10}$  BB unit on the vertical axis. This is due to the reduction in chemical space generated by the transferable coarse-grained model: from Fig. S8 it is apparent that chemically different compounds mapping to the same coarse-grained representation exhibit similar permeation

properties (in terms of  $\log_{10} BB$ ).

The accuracy of CG models when increasing the molecular weight is again remarkable, with an exception in the case of Salbutamol (“Salb” in Fig. S8). The presence of this outlier is connected to Martini parametrization issues for some high molecular-weight compounds containing ring structures, a problem currently under investigation.

## S9. GROMACS INPUT FILES

In this section we report the GROMACS input files for the set of small molecules (extracted from Ref. 6) investigated by means of coarse-grained simulations: Atenolol, Cimetidine, Ibuprofen, Mannitol, Salbutamol and Salicylate.

---

atenolol.itp

---

```
; GENERATED WITH auto_martini.py
; Atenolol
; Tristan Bereau 2014

[moleculetype]
; molname      nrexcl
MOL            2

[atoms]
; id  type  resnr  residue  atom  cgnr  charge  smiles
; 1   P2    1     MOL     P01   1     0       ; CCN=O
; 2   SC5   1     MOL     S01   2     0       ; c1ccccc1
; 3   SC5   1     MOL     S02   3     0       ; c1ccccc1
; 4   SC5   1     MOL     S03   4     0       ; c1ccccc1
; 5   P2    1     MOL     P02   5     0       ; CO
; 6   P3    1     MOL     P03   6     0       ; NCCO
; 7   C2    1     MOL     C01   7     0       ; CCC

[bonds]
; i j      funct  length  force.c.
; 1 2      1      0.25   1250
; 4 5      1      0.37   1250
; 5 6      1      0.26   1250
; 6 7      1      0.24   1250

[constraints]
; i j      funct  length
; 2 3      1      0.24
; 2 4      1      0.24
; 3 4      1      0.24

[angles]
; i j k      funct  angle  force.c.
; 1 2 3      2      128.1  25.0
; 1 2 4      2      143.7  25.0
; 2 4 5      2      114.0  25.0
; 3 4 5      2      54.2   25.0
; 4 5 6      2      83.6   25.0
; 5 6 7      2      117.2  25.0
```

---

```
; GENERATED WITH auto_martini.py
; Cimetidine
; Tristan Bereau 2014

[moleculetype]
; molname      nrexcl
MOL            2

[atoms]
; id  type      resnr  residue  atom  cgnr  charge  smiles
  1   SNd       1     MOL     S01   1     0     ; Cc1cncn1
  2   SP1       1     MOL     S02   2     0     ; c1cncn1
  3   NO        1     MOL     N01   3     0     ; CS
  4   C5        1     MOL     C01   4     0     ; CC
  5   P2        1     MOL     P01   5     0     ; CN=CN
  6   P2        1     MOL     P02   6     0     ; NC#N

[bonds]
; i j      funct  length  force.c.
  2 3       1      0.25   1250
  3 4       1      0.27   1250
  4 5       1      0.31   1250
  5 6       1      0.25   1250

[constraints]
; i j      funct  length
  1 2       1      0.22

[angles]
; i j k      funct  angle  force.c.
  1 2 3       2      65.5   25.0
  2 3 4       2      86.2   25.0
  3 4 5       2     152.0   25.0
  4 5 6       2      94.1   45.0
```

```
; GENERATED WITH auto_martini.py
; Ibuprofen
; Tristan Bereau 2014

[moleculetype]
; molname      nrexcl
MOL            2

[atoms]
; id  type  resnr  residue  atom  cgnr  charge  smiles
  1   C3    1     MOL     C01   1     0       ; CCCC
  2   SC5   1     MOL     S01   2     0       ; c1ccccc1
  3   SC5   1     MOL     S02   3     0       ; c1ccccc1
  4   SC5   1     MOL     S03   4     0       ; c1ccccc1
  5   Nda   1     MOL     N01   5     0       ; CCCO=O

[bonds]
; i j      funct  length  force.c.
  1 4      1       0.34   1250
  3 5      1       0.25   1250

[constraints]
; i j      funct  length
  2 3      1       0.24
  2 4      1       0.24
  3 4      1       0.24

[angles]
; i j k      funct  angle  force.c.
  1 4 2      2       69.2   25.0
  1 4 3      2       123.3  25.0
  2 3 5      2       144.4  25.0
  4 3 5      2       128.0  25.0
```

---

mannitol.itp
--------------

---

```
;;; GENERATED WITH auto-martini  
; Mannitol  
; Tristan Bereau 2014
```

```
[moleculetype]  
; molname      nrexcl  
MOL            2
```

```
[atoms]  
; id  type  resnr  residu  atom  cgnr  charge  smiles  
  1   P4    1     MOL    P01   1     0       ; OCCOCO  
  2   P4    1     MOL    P02   2     0       ; OCCOCO
```

```
[bonds]  
; i j  funct  length  force.c.  
  1  2    1     0.26   1250
```

---

---

salbutamol.itp
----------------

---

```
; GENERATED WITH auto_martini.py
; Salbutamol
; Tristan Bereau 2014
```

```
[moleculetype]
```

```
; molname      nrexcl
MOL             2
```

```
[atoms]
```

```
; id  type    resnr  residue  atom  cgnr  charge  smiles
  1   P2      1     MOL    P01   1     0     ; CO
  2   SC5     1     MOL    S01   2     0     ; c1ccccc1
  3   SC5     1     MOL    S02   3     0     ; c1ccccc1
  4   SNda    1     MOL    S03   4     0     ; Oc1ccccc1
  5   P1      1     MOL    P02   5     0     ; CO
  6   Nd      1     MOL    N01   6     0     ; CCCCN
```

```
[bonds]
```

```
; i j    funct  length  force.c.
  1 2     1      0.25   1250
  3 5     1      0.25   1250
  5 6     1      0.35   1250
```

```
[constraints]
```

```
; i j    funct  length
  2 3     1      0.24
  2 4     1      0.24
  3 4     1      0.24
```

```
[angles]
```

```
; i j k    funct  angle  force.c.
  1 2 3     2     121.3  25.0
  1 2 4     2     61.3   25.0
  2 3 5     2     61.3   25.0
  3 5 6     2    118.2  25.0
  4 3 5     2     121.5  25.0
```

---

```
; GENERATED WITH auto_martini.py
; Salicylate
; Tristan Bereau 2014

[moleculetype]
; molname      nrexcl
MOL            2

[atoms]
; id  type    resnr  residue  atom  cgnr  charge  smiles
  1   SC5     1     MOL     S01   1     0     ; c1ccccc1
  2   SNda    1     MOL     S02   2     0     ; Oc1ccccc1
  3   SC5     1     MOL     S03   3     0     ; c1ccccc1
  4   P1      1     MOL     P01   4     0     ; OC=O

[bonds]
; i j      funct  length  force.c.
  3 4       1      0.25    1250

[constraints]
; i j      funct  length
  1 2       1      0.24
  1 3       1      0.24
  2 3       1      0.24

[angles]
; i j k      funct  angle  force.c.
  1 3 4       2     122.0  25.0
  2 3 4       2     62.0   25.0
```

---

```
; GENERATED WITH auto_martini.py
; Benzoic acid
; Tristan Bereau 2014
```

```
[moleculetype]
; molname      nrexcl
MOL            2
```

```
[atoms]
; id  type  resnr  residue  atom  cgnr  charge  smiles
  1   P1    1     MOL     P01   1     0       ; OC=O
  2   SC5   1     MOL     S01   2     0       ; c1ccccc1
  3   SC5   1     MOL     S02   3     0       ; c1ccccc1
  4   SC5   1     MOL     S03   4     0       ; c1ccccc1
```

```
[bonds]
; i j  funct  length  force.c.
  1 4    1     0.25   1250
```

```
[constraints]
; i j  funct  length
  2 3    1     0.24
  2 4    1     0.24
  3 4    1     0.24
```

```
[angles]
; i j k  funct  angle  force.c.
  1 4 2    2     61.5   25.0
  1 4 3    2    121.5   25.0
```

---

---

urea.itp
----------

---

```
; GENERATED WITH auto_martini.py
; Urea
; Tristan Bereau 2014
```

```
[moleculetype]
; molname      nrexcl
MOL            2
```

```
[atoms]
; id  type  resnr  residue  atom  cgnr  charge  smiles
  1   P4    1     MOL     P01   1      0      ; NCN=O
```

---

## S10. FUNCTIONAL GROUP DISTRIBUTIONS

In this section we provide the statistics for the top five most populous functional groups found in each highlighted region in Fig. 3 of the main text. For clarity, we reinsert a modified version of the figure below, with each region labeled with a number. The numbers correspond to entries in the tables detailing the total number of molecules and functional group populations found in each region. The instances of each functional group are detected using the CHECKMOL package [15], which also provides the definition of each functional group in its documentation. Note that we no longer color the points by their permeabilities, rather we use the number of heteroatom substitutions in each molecule. Zero corresponds to molecules made only of carbons (saturated with hydrogens), while larger heteroatom substitutions incorporate oxygens, nitrogens, and fluorines. Unsurprisingly, we find that the number of heteroatom substitutions acts as a good proxy for water/octanol partitioning, making the compounds increasingly polar.

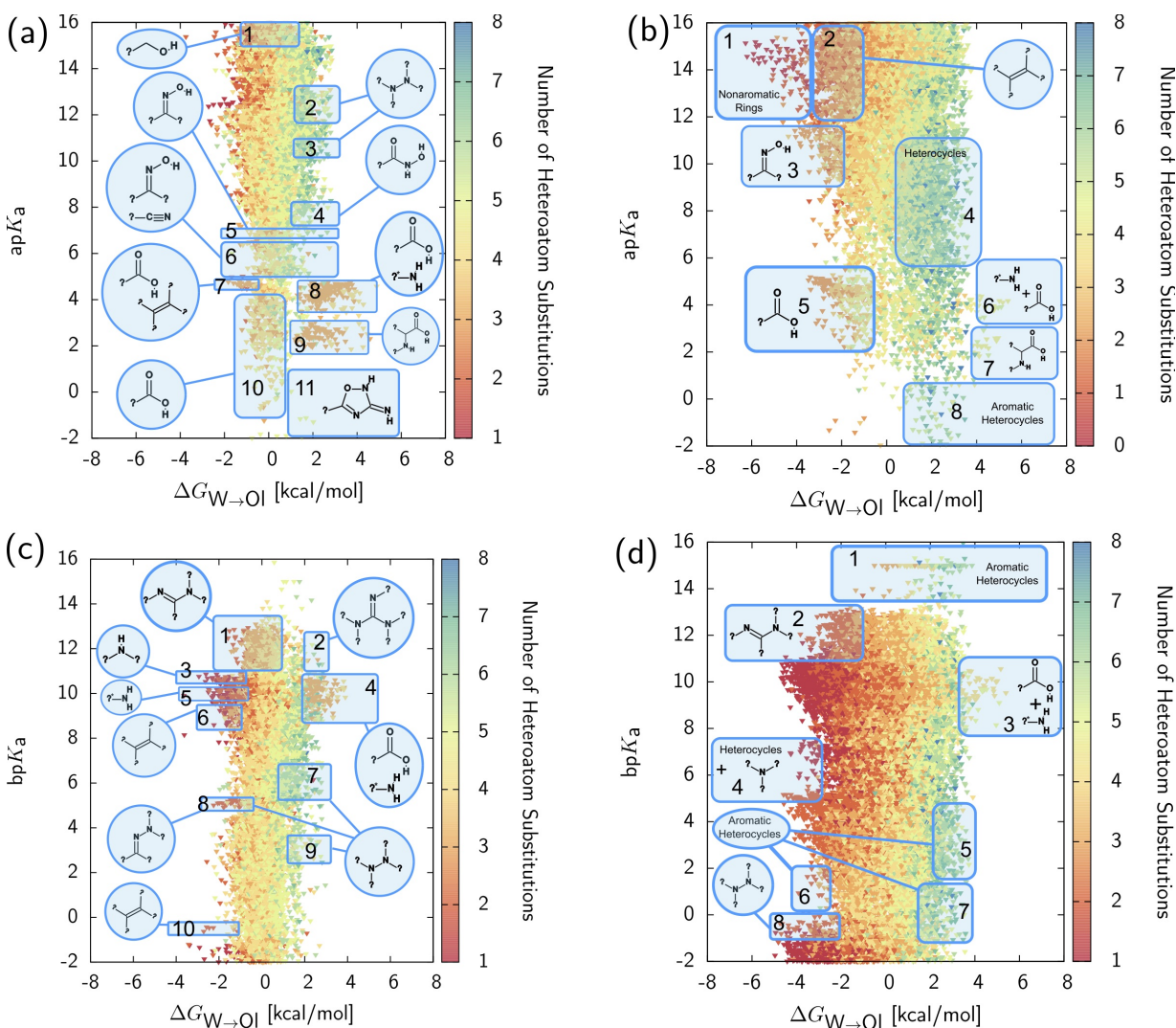


FIG. S9. Adaptation of Fig. 3 (main text) with each blue highlighted region labeled with a number. Acidic and basic pKa are shown in panels (a,b) and (c,d), respectively. Panels (a,c) and (b,d) describe the coverage corresponding to coarse-grained unimers and dimers, respectively. The numbers of each region correspond to rows in the tables below that specify the percentage of the molecules containing specific functional groups. The points are now colored based on the number of heteroatom substitutions per molecule.

TABLE S2. Table detailing top two functional group populations for regions highlighted in Fig. S9a.

Region #	Total Molecules	FG 1, %	FG 2, %
1	7231	prim. alcohol, 58.5	alkene, 38.3
2	493	hydrazine, 50.1	nitrile, 21.3
3	275	hydrazine, 50.2	carboxylic acid sec. amide, 21.5
4	145	hydroxamic acid, 51.0	nitrile, 25.5
5	367	oxime, 57.0	nitrile, 36.0
6	788	oxime, 53.7	nitrile, 52.9
7	90	carboxylic acid, 78.9	alkene, 53.3
8	461	carboxylic acid, 97.8	prim. aliphatic amine, 72.7
9	271	carboxylic acid, 92.3	alpha-aminoacid, 59.8
10	1187	carboxylic acid, 80.9	alkyne, 36.5
11	12	iminohetarene, 91.7	aromatic compound, 91.7

TABLE S3. Continuation of table S1, detailing top third through fifth functional group populations for regions highlighted in Fig. S9a.

Region #	FG 3, %	FG 4, %	FG 5, %
1	alkyne, 21.2	hydrazine, 18.8	nitrile, 16.1
2	sec. alcohol, 20.9	prim. alcohol, 17.6	alkyne, 14.4
3	nitrile, 20.0	alkyne, 16.4	urea, 10.2
4	hydrazine, 22.1	aldehyde, 15.2	oxime, 14.5
5	alkyne, 30.0	alkyl fluoride, 15.8	ketone, 12.8
6	alkyne, 27.3	alkyl fluoride, 18.9	aldehyde, 17.1
7	alkyl fluoride, 25.6	prim. alcohol, 14.4	hydrazine, 13.3
8	alkene, 58.8	sec. aliphatic amine, 24.5	alkyne, 13.9
9	prim. aliphatic amine, 49.1	alkene, 39.1	sec. aliphatic amine, 35.8
10	nitrile, 28.1	alkene, 25.9	oxime, 14.3
11	heterocyclic compound, 91.7	aldehyde, 33.3	alkyne, 33.3

TABLE S4. Table detailing top two functional group populations for regions highlighted in Fig. S9b.

Region #	Total Molecules	FG 1, %	FG 2, %
1	201	nonaromatic ring, 99.5	alkene, 99.5
2	3769	alkene, 70.3	alkyne, 42.1
3	724	oxime, 65.9	alkene, 65.3
4	17068	heterocyclic compound, 49.6	aromatic compound, 41.4
5	1914	carboxylic acid, 79.8	alkene, 56.6
6	215	carboxylic acid, 83.3	prim. aliphatic amine, 66.0
7	172	carboxylic acid, 85.5	alpha-aminoacid, 69.2
8	668	aromatic compound, 97.9	heterocyclic compound, 97.9

TABLE S5. Continuation of table S3, detailing top third through fifth functional group populations for regions highlighted in Fig. S9b.

Region #	FG 3, %	FG 4, %	FG 5, %
1	alkyne, 8.5	halogen deriv., 8.0	alkyl fluoride, 2.0
2	alkyl fluoride, 25.3	prim. alcohol, 16.5	sec. alcohol, 16.1
3	alkyne, 36.3	alkyl fluoride, 14.8	heterocyclic compound, 9.9
4	iminohetarene, 23.4	oxohetarene, 18.5	hydrazine, 18.4
5	alkyl fluoride, 24.1	alkyne, 20.2	heterocyclic compound, 13.5
6	sec. aliphatic amine, 30.2	heterocyclic compound, 26.5	aromatic compound, 17.2
7	sec. aliphatic amine, 56.4	prim. aliphatic amine, 51.7	heterocyclic compound, 27.3
8	iminohetarene, 96.3	hydrazine 25.1	phenol, 23.4

TABLE S6. Table detailing top two functional group populations for regions highlighted in Fig. S9c.

Region #	Total Molecules	FG 1, %	FG 2, %
1	3651	carboxylic acid amidine, 61.3	alkene, 36.5
2	66	guanidine, 63.6	hydrazine, 42.4
3	356	sec. aliphatic amine, 55.3	alkene, 48.9
4	778	carboxylic acid, 68.5	prim. aliphatic amine, 59.5
5	636	alkene, 66.8	prim. aliphatic amine, 57.9
6	626	alkene, 63.4	prim. aliphatic amine, 48.9
7	2439	hydrazine, 61.3	nitrile, 19.0
8	123	hydrazine, 75.6	hydrazine, 60.2
9	302	hydrazine, 74.8	carboxylic acid hydrazide, 26.5
10	32	hydrazine, 62.5	alkene, 56.3

TABLE S7. Continuation of table S5, detailing top third through fifth functional group populations for regions highlighted in Fig. S9c.

Region #	FG 3, %	FG 4, %	FG 5, %
1	enamine, 22.5	guanidine, 20.1	hydrazine, 16.6
2	carboxylic acid amidine, 19.7	carboxylic acid, 16.7	prim. alcohol, 13.6
3	prim. aliphatic amine, 44.1	alkyl fluoride, 24.7	alkyne, 11.8
4	alkene, 40.62	sec. aliphatic amine, 17.7	hydrazine, 16.2
5	sec. aliphatic amine, 34.1	alkyl fluoride, 29.7	alkyne, 16.8
6	alkyne, 33.4	sec. aliphatic amine, 30.2	alkyl fluoride, 27.8
7	alkyne, 15.9	carboxylic acid amidrazone, 10.0	prim. alcohol, 10.0
8	alkene, 43.1	alkyne 18.7	nitrile, 9.8
9	semicarbazide, 22.8	prim. alcohol, 14.6	alkyne, 13.9
10	alkyne, 25.0	nitrile, 12.5	oxime, 9.4

TABLE S8. Table detailing top two functional group populations for regions highlighted in Fig. S9d.

Region #	Total Molecules	FG 1, %	FG 2, %
1	768	heterocyclic compound, 90.5	aromatic compound, 88.3
2	3599	carboxylic acid amidine, 71.3	alkene, 53.0
3	688	prim. aliphatic amine, 82.3	carboxylic acid, 72.1
4	778	heterocyclic compound, 94.9	tert. aliphatic amine, 75.9
5	1508	heterocyclic compound, 69.5	aromatic compound, 63.3
6	91	aromatic compound, 76.9	heterocyclic compound, 76.9
7	2528	heterocyclic compound, 65.4	aromatic compound, 57.0
8	291	hydrazine, 68.0	alkene, 58.1

TABLE S9. Continuation of table S7, detailing top third through fifth functional group populations for regions highlighted in Fig. S9d.

Region #	FG 3, %	FG 4, %	FG 5, %
1	iminohetarene, 86.1	phenol, 27.6	hydrazine, 15.6
2	enamine, 18.8	heterocyclic compound, 17.0	alkyl fluoride, 11.0
3	alpha-aminoacid, 28.5	sec. aliphatic amine, 23.8	alkene, 15.6
4	alkene, 55.7	alkyne, 21.7	sec. aliphatic amine, 16.1
5	hydrazine, 50.1	oxohetarene, 37.7	iminohetarene, 34.8
6	alkene, 52.7	alkyne, 22.0	oxime ether, 8.8
7	iminohetarene, 34.8	oxohetarene, 31.8	hydrazine, 29.6
8	tert. alcohol, 22.7	alkyne 10.0	sec. alcohol, 6.5

- 
- [1] Votapka, L. W.; Lee, C. T.; Amaro, R. E., Two relations to estimate membrane permeability using milestoning, *J. Phys. Chem. B* **2016**, *120*, 8606–8616.
  - [2] Marrink, S. J.; de Vries, A. H.; Mark, A. E., Coarse grained model for semiquantitative lipid simulations, *J. Phys. Chem. B* **2004**, *108*, 750–760.
  - [3] Marrink, S. J.; Risselada, H. J.; Yefimov, S.; Tieleman, D. P.; de Vries, A. H., The MARTINI force field: coarse grained model for biomolecular simulations, *J. Phys. Chem. B* **2007**, *111*, 7812–7824.
  - [4] Marrink, S. J.; Tieleman, D. P., Perspective on the Martini model, *Chem. Soc. Rev.* **2013**, *42*, 6801–6822.
  - [5] Rudzinski, J. F.; Kremer, K.; Bereau, T., Communication: Consistent interpretation of molecular simulation kinetics using Markov state models biased with external information, *J. Chem. Phys.* **2016**, *144*, 051102.
  - [6] Carpenter, T. S.; Kirshner, D. A.; Lau, E. Y.; Wong, S. E.; Nilmeier, J. P.; Lightstone, F. C., A method to predict blood-brain barrier permeability of drug-like compounds using molecular dynamics simulations, *Biophys. J.* **2014**, *107*, 630–641.
  - [7] Lee, C. T.; Comer, J.; Herndon, C.; Leung, N.; Pavlova, A.; Swift, R. V.; Tung, C.; Rowley, C. N.; Amaro, R. E.; Chipot, C.; Wang, Y.; Gumbard, J. C., Simulation-based approaches for determining membrane permeability of small compounds, *J. Chem. Inf. Model.* **2016**, *56*, 721–733.
  - [8] Bereau, T.; Kremer, K., Automated parametrization of the coarse-grained Martini force field for small organic molecules, *J. Chem. Theory Comput.* **2015**, *11*, 2783–2791.
  - [9] MacCallum, J. L.; Bennett, W. D.; Tieleman, D. P., Distribution of amino acids in a lipid bilayer from computer simulations, *Biophys. J.* **2008**, *94*, 3393–3404.
  - [10] Tetko, I. V.; Tanchuk, V. Y., Application of associative neural networks for prediction of lipophilicity in ALOGPS 2.1 program, *J. Chem. Inf. Comput. Sci.* **2002**, *42*, 1136–1145.
  - [11] Menichetti, R.; Kanekal, K. H.; Kremer, K.; Bereau, T., In silico screening of drug-membrane thermodynamics reveals linear relations between bulk partitioning and the potential of mean force, *J. Chem. Phys.* **2017**, *147*, 125101.
  - [12] Calculator Plugin of ChemAxon Marvin 17.28.0 **2017**.
  - [13] Wichmann, K.; Diedenhofen, M.; Klamt, A., Prediction of blood-brain partitioning and human serum albumin binding based on COSMO-RS  $\sigma$ -moments, *J. Chem. Inf. Model.* **2007**, *47*, 228–233.
  - [14] Bennion, B. J.; Be, N. A.; McNERney, M. W.; Lao, V.; Carlson, E. M.; Valdez, C. A.; Malfatti, M. A.; Enright, H. A.; Nguyen, T. H.; Lightstone, F. C.; Carpenter, T. S., Predicting a drug's membrane permeability: A computational model validated with in vitro permeability assay data, *J. Phys. Chem. B* **2017**, *121*, 5228–5237.
  - [15] Haider, N., Functionality pattern matching as an efficient complementary structure/reaction search tool: An open-source approach, *Molecules* **2010**, *15*, 5079–5092.